

# Lattice Multislice Algorithm for Fast Simulation of Scanning Transmission Electron Microscopy Images

Christian Doberstein and Peter Binev \*

October 26, 2023

**Abstract:** We introduce a new approach to the numerical simulation of the Scanning Transmission Electron Microscopy images. The Lattice Multislice Algorithm (LMA) takes advantage of the fact that the electron waves passing through the specimen have limited bandwidth and therefore can be approximated very well by a low-dimensional linear space spanned by translations of a well-localized function  $u$ . Just like in the PRISM algorithm recently published by C. Ophus, we utilize the linearity of the Schrödinger equation, but perform the approximations with functions that are well localized in real space instead of Fourier space. This way, we achieve a similar computational speedup as PRISM, but at a much lower memory consumption and reduced numerical error due to avoiding virtual copies of the probe waves interfering with the result. Our approach also facilitates faster recomputations if local changes are made to the specimen such as changing a single atomic column.

## 1 Introduction

The simulation of scanning transmission electron microscopy (STEM) images is frequently necessary for a correct interpretation of the experimental data. Unfortunately, STEM image simulation is a computationally highly demanding task. Depending on specimen complexity and desired resolution, the simulation of a single STEM image may take many hours or even days to complete [1]. If multiple images need to be simulated for different atomic configurations, this task quickly becomes infeasible.

At its core, the problem is that a partial differential equation (PDE) needs to be solved many times. For STEM imaging, the relativistically correct PDE describing the transmission of an electron wave through the electrostatic potential of a specimen is

---

\*This research was supported in part by the ARO grant W911NF-20-1-0318 and the NSF Grants DMS 2038080, DMS 1925919, and DMS 2245097.

given by the Dirac equation. In it, the electron wave is represented by a function with values in a four-dimensional complex space and its computation is not practical. The commonly used approximation for the electron wave is a single complex-valued function solving the Schrödinger equation for fast electrons [6].

For the purpose of STEM image simulation, the initial conditions to the PDE typically represent different positions of the STEM probe, each of which corresponds to a single pixel in the two dimensional output image. In order to account for thermal diffuse scattering (TDS) caused by thermal vibrations of the atoms and partial coherence of the STEM probes, the entire simulation is repeated several times with slightly different probe and specimen parameters and the results are averaged. In the standard *multislice algorithm* [6, 2] for example, the Schrödinger equation needs to be solved several times for the computation of one pixel of the resulting STEM image. Consequently, even for a small output image sampled at  $256 \times 256$  pixels, this results in having to solve the Schrödinger equation millions of times.

There has been some progress lately on accelerating these computations. A straightforward approach is to limit the size of the computation window to a small region around the center of the individual STEM probes. This way, the Schrödinger equation only needs to be solved on an area that may be much smaller than the entire specimen area. This provides good approximations to the true solution due to the relatively fast decay of focused STEM probes and yields a speed up of approximately  $f^2$  compared to the standard multislice algorithm if the size of the simulation window is reduced by a factor of  $f$  in both directions. There is a rumour about MULTEM [9, 8] implementing this approach, but it is not mentioned in the corresponding publications. MULTEM also comprises a higher order expansion of the multislice split-step solution and an efficient implementation on the GPU. STEMSalabim [10] is a recent implementation of the standard Multislice algorithm that achieves short computation times via distributed computing using MPI.

The PRISM algorithm [11] and its implementation Prismatic [5, 3] take a very different approach. Instead of propagating the STEM probes themselves through the specimen, PRISM utilizes the linearity of the Schrödinger equation and propagates certain exponential functions through the specimen, which are given by Dirac deltas in Fourier space. The probes are then approximated by linear combinations of these Dirac deltas, which gives the corresponding solutions to the Schrödinger equation due to its linearity. One advantage of this approach is the fact that the frequencies of the STEM probes are limited by the objective aperture, which typically results in a smaller number of Dirac deltas than STEM probe positions. An additional advantage is that it is possible to consider only every  $f$ -th Dirac delta in  $x$  and  $y$  directions after the discretization, thereby reducing by  $f^2$  the number of times that the Schrödinger equation needs to be solved at a negligible loss of accuracy for small  $f$ . Since additionally only those exponential functions that correspond to frequencies within the (potentially small) objective aperture need to be considered, this method achieves shorter computation times than the simple reduction of the simulation window size by a factor of  $f^2$ .

Here, we present a new method based on the idea of PRISM. Instead of using functions that are localized in Fourier space such as the Dirac deltas of PRISM, we consider

functions that are localized in real space coordinates for the approximation of the STEM probes. This has several advantages on which we will elaborate in more detail in this paper: (i) it reduces the numerical error in the probe approximation, (ii) avoids an excessive memory consumption for large specimen, and (iii) reduces the required amount of additional computations if local changes are made to the specimen structure. At the same time, we are able to keep the benefits of PRISM. In particular, a similar computational speedup is achieved and we keep the ability to flexibly trade off computation time against accuracy by means of several parameters described in Section 4.2.

There exists a multitude of codes for electron microscopy simulation that serve various purposes, many of which are freely available online. Aside from the algorithms mentioned above, lists with additional references can be found in [5, 7, 6].

## 2 Introduction to LMA

Lattice Multislice Algorithm (LMA) utilizes translations of a special initial wave  $u$  for which a variant of the *multislice algorithm* (see Subsection 3.2) is applied. Given a set  $\mathcal{I}$  of shift positions  $i \in \mathcal{I}$  (considered in Subsection 4.2.1), we obtain a set of initial waves  $u_i := u(\cdot - i)$  that are used to approximate the initial waves of the probes  $\psi_p^{\text{init}}$  for  $p \in \mathcal{P}$ . Here  $\mathcal{P}$  is the set of probe positions for which we want to calculate  $\hat{\psi}_p^{\text{exit}}$ , see Subsection 3.1. The calculations of the electron wave propagation are performed on a rectangular grid of  $X \times Y$  points (see Section 4). For convenience,  $\mathcal{P}$  can be taken to be a subset of this grid, while  $\mathcal{I}$  is often a subset of  $\mathcal{P}$ . The number of elements of these sets usually satisfy the inequalities  $|\mathcal{I}| < |\mathcal{P}| < XY$ , although  $|\mathcal{I}| \geq |\mathcal{P}|$  is also possible.

In contrast, PRISM approximates the probes via linear combinations of a set  $\mathcal{K}$  of elementary waves represented by Dirac deltas in Fourier space (see Subsection 4.1). The set  $\mathcal{K}$  is uniquely determined by the aperture function  $A(k)$  from (4) and the discretization provided by the  $X \times Y$  grid in real space. This discretization fixes the scaling of  $k$  the Fourier space and determines the number of elementary waves that is limited by the number of discrete points  $k$  satisfying  $\|k\| < k_{\text{max}}$ .

The linear space  $\text{span}(\mathcal{K})$  of the linear combinations of the elementary waves from  $\mathcal{K}$  is  $|\mathcal{K}|$ -dimensional and approximates the probes extremely well. This indicates the feasibility of finding a linear space of dimension  $|\mathcal{K}|$  or slightly larger that approximates the probes very well. In LMA we represent this space as the linear combinations  $\text{span}(u_i, i \in \mathcal{I})$  of  $u_i$  using different options for  $u$ . Standard choices for  $u$  are an initial probe wave or a Gaussian, both considered in Subsection 4.2.3. Other options are also discussed there. One of them establishes a direct theoretical link between PRISM and LMA. It is based on a special representation of  $u$  as a tensor product of univariate trigonometric polynomials.

In one dimension, the elementary waves  $e^{ikt}$  are the Dirac deltas at the discrete points in Fourier space. The trigonometric polynomials  $\mathcal{T}_n$  are the linear subspace of the space of  $2\pi$ -periodic functions spanned by  $e^{ikt}$  for  $k = -n, -n + 1, \dots, n$ . An alternative basis of  $\mathcal{T}_n$  is the set of translations  $\varphi_n(t - \frac{2\pi j}{2n+1})$  for  $j = -n, -n + 1, \dots, n$  of the trigonometric

polynomial

$$\varphi_n(t) = \sum_{k=-n}^n e^{ikt} \cos\left(\frac{k\pi}{2n+2}\right) \quad (1)$$

defined in [12]. Let  $W$  be the  $(2n+1) \times (2n+1)$  modulation matrix with entries  $W_{k,j} = e^{-\frac{2\pi jk}{2n+1}}$ . Then the  $(2n+1) \times (2n+1)$  transformation matrix  $M$  from the basis of the elementary waves to the translations of the localized trigonometric polynomial from (1) is

$$M = W \text{diag}\left(\cos\left(\frac{k\pi}{2n+2}\right)\right),$$

where  $\text{diag}(a_k)$  is the diagonal matrix with entries  $a_k$  on the main diagonal. Using that  $\frac{1}{2n+1}W$  is a Hermitian matrix, it is easy to see that

$$M^{-1} = \frac{1}{(2n+1)^2} \text{diag}\left(1/\cos\left(\frac{k\pi}{2n+2}\right)\right) W^*,$$

where  $W^* = \bar{W}^T$  is the conjugate transpose of  $W$ . Matrices  $M$  and  $M^{-1}$  provide easy transformations from one basis to another in one dimension.

To use the above framework in two dimensions we define  $u(x, y) := \varphi_n(x)\varphi_n(y)$  to be the tensor product of localized trigonometric polynomials in each direction. This allows an easy transition from the global elementary waves to localized waves using the matrices  $M$  and  $M^{-1}$ . A minor inconvenience is the fact that instead of the set  $\mathcal{K}$  of elementary waves related to the points  $k = (k_x, k_y)$  satisfying  $\|k\| = \sqrt{k_x^2 + k_y^2} \leq n$  we now consider a larger set  $\mathcal{K}_+$  related to  $k$  satisfying  $|k_x| \leq n$  and  $|k_y| \leq n$  to receive the set  $\mathcal{I}$  of translations  $i$  of localized waves  $u_i$  with  $|\mathcal{I}| = |\mathcal{K}_+| \approx 4n^2$  compared to  $|\mathcal{K}| \approx \pi n^2$ . However, this setup provides more symmetries and less complicated implementation. In particular, the representations of the probes via linear combinations of the translations  $u_i$  of  $u$  are received from the ones for the elementary waves by multiplications by  $M^{-1}$ . It should be noted that starting from  $\text{span}(\mathcal{K}_f)$  one can receive in a similar way a corresponding generating function  $u_f$  for a reduced set of translations  $\mathcal{I}_f$ .

### 3 Background

We briefly summarize the most relevant steps of STEM image formation and the standard Multislice algorithm and introduce the notation used in the rest of the paper. A much more detailed description of the standard algorithms for STEM image simulation can be found in the book by Kirkland [6].

#### 3.1 STEM image formation

In STEM, an image is formed by scanning a specimen one point at a time. The scanning positions are arranged on a standard lattice and at each of these positions a focused STEM probe is transmitted through the specimen and recorded subsequently after exiting the specimen. The detector has the shape of an annulus or a disk and records the

squared magnitude of the electron wave in Fourier space. It is possible to record the squared magnitude of the entire electron wave as a pixelated image (4D STEM), the integrated values on many small annuli (3D STEM) or the integrated value over one large annulus or disk (2D STEM).

For a given probe position  $p \in \mathbb{R}^2$ , the STEM output is generated in three steps as follows.

1. A focused STEM probe is formed at the position  $p$  on the surface of the specimen. The probe wave function is given by

$$\psi_p^{\text{init}}(x) = \mathcal{F}^{-1}(\exp(-i\chi)A)(x - p) \quad \forall x \in \mathbb{R}^2, \quad (2)$$

where  $\mathcal{F}^{-1}$  is the inverse Fourier transform and  $\chi : \mathbb{R}^2 \rightarrow \mathbb{R}$  is the wave aberration function

$$\chi(k) = \frac{1}{2}\pi C_s \lambda^3 \|k\|_2^4 - \pi Z \lambda \|k\|_2^2 \quad \forall k \in \mathbb{R}^2 \quad (3)$$

with third order spherical aberration  $C_s \in \mathbb{R}$ , focus  $Z \in \mathbb{R}$  and electron wavelength  $\lambda > 0$ . The aperture function  $A$  acts as an ideal lowpass filter on the STEM probe and is defined as

$$A(k) = \mathbb{1}_{B_{\alpha_{\max}/\lambda}(0)}(k) = \begin{cases} 1, & \lambda \|k\|_2 < \alpha_{\max}, \\ 0, & \text{otherwise} \end{cases} \quad \forall k \in \mathbb{R}^2, \quad (4)$$

where  $\alpha_{\max} > 0$  is the maximum semiangle allowed by the objective aperture. For simplicity, no higher order or anisotropic aberrations have been included in the wave aberration function. The precise form of the aberration function used does not affect the results presented in this paper.

2. The probe is transmitted through the specimen. Although not relativistically correct, the transmission is commonly modeled by the Schrödinger equation for fast electrons,

$$\frac{\partial \psi(r)}{\partial z} = \frac{i\lambda}{4\pi} \Delta_{xy} \psi(r) + i\sigma V(r) \psi(r) \quad \forall r = (x, y, z) \in \mathbb{R}^3, \quad (5)$$

with  $\psi_p^{\text{init}}$  from step 1 as the initial condition at the entrance plane of the specimen,

$$\psi(x, y, 0) = \psi_p^{\text{init}}(x, y) \quad \forall (x, y) \in \mathbb{R}^2.$$

Here,  $\Delta_{xy} = \frac{\partial^2}{\partial x^2} + \frac{\partial^2}{\partial y^2}$  is the two dimensional Laplace operator,  $\sigma > 0$  is the beam sample interaction constant and  $V : \mathbb{R}^3 \rightarrow \mathbb{R}_{>0}$  is the electrostatic potential of the specimen. The electron wave at the exit plane of the specimen, also called exit wave, is denoted by  $\psi_p^{\text{exit}}(x, y) := \psi_p(x, y, t)$ , where  $\psi_p$  is the solution to the Schrödinger equation with initial condition  $\psi_p^{\text{init}}$  and  $t > 0$  is the specimen thickness.

3. A detector records the squared amplitude of the exit wave in Fourier space. The final STEM output for the probe position  $p$  is then given as

$$\begin{aligned}
\text{4D STEM:} & \quad \left( \left| \mathcal{F}(\psi_p^{\text{exit}})(ad_x + bd_y) \right|^2 \right)_{\substack{a=-A, \dots, A \\ b=-B, \dots, B}} \quad (A, B \in \mathbb{N}, d_x, d_y > 0) \\
\text{3D STEM:} & \quad \left( \int_{B_{(a+1)r}(0) \setminus B_{ar}(0)} |\mathcal{F}(\psi_p^{\text{exit}})(k)|^2 dk \right)_{a=0, \dots, A} \quad (A \in \mathbb{N}, r > 0) \\
\text{2D STEM:} & \quad \int_{B_{r_2}(0) \setminus B_{r_1}(0)} |\mathcal{F}(\psi_p^{\text{exit}})(k)|^2 dk, \quad (r_1, r_2 \geq 0)
\end{aligned}$$

where  $\mathcal{F}$  is the (forward) Fourier transform.

The collection of the pixel values in step 3 for all probe positions  $p$  forms the 2D, 3D or 4D STEM image. The probe positions generally lie on a rectangular standard lattice and are contained within a rectangular domain corresponding to the specimen area of which a STEM image is simulated, referred to as the simulation domain in the following. The simulation domain is usually assumed to be periodic because of the use of the discrete Fourier transform (DFT) in the Multislice algorithm.

The description of STEM image formation given above assumes a perfectly coherent illumination and a completely static specimen. In reality, the illumination in a STEM is only partially coherent and the atoms in the specimen vibrate slightly so that the specimen potential  $V$  is not constant for the entire duration of image acquisition. In order to account for these effects, steps 1 to 3 are typically repeated several times with slightly different probe wave functions  $\psi_p^{\text{init}}$  and specimen potentials  $V$ . In the end, these results are averaged to compute the final STEM image.

### 3.2 The Multislice Algorithm

Steps 1 and 3 above can be easily computed, while solving the Schrödinger equation in step 2 is computationally more demanding. The Schrödinger equation is generally solved with the Multislice algorithm, which is a split-step method similar to the Euler method. Another popular method, the Bloch wave method, requires solving a large eigenvalue/eigenvector problem and is feasible only for very small specimen [6].

In the Multislice algorithm, the specimen is divided into thin slices along the beam direction  $z$  and the Schrödinger equation (5) is split into two parts, the propagation term  $\frac{i\lambda}{4\pi} \Delta_{xy} \psi(r)$  and the transmission term  $i\sigma V(r) \psi(r)$ . This yields an approximate solution to the Schrödinger equation by alternately multiplying the electron wave with the transmission function

$$t_z(x, y) := \exp \left( i\sigma \underbrace{\int_z^{z+\varepsilon} V(x, y, z') dz'}_{=: v_\varepsilon(x, y, z)} \right) = \exp(i\sigma v_\varepsilon(x, y, z)) \quad \forall x, y \in \mathbb{R}^2$$

and convolving it with the propagation function

$$q(x, y) := \frac{-i}{\lambda\varepsilon} \exp\left(\frac{i\pi}{\lambda\varepsilon}(x^2 + y^2)\right) \quad \forall x, y \in \mathbb{R}^2,$$

where  $\varepsilon > 0$  is the slice thickness. The Multislice algorithm is summarized in Figure 1.

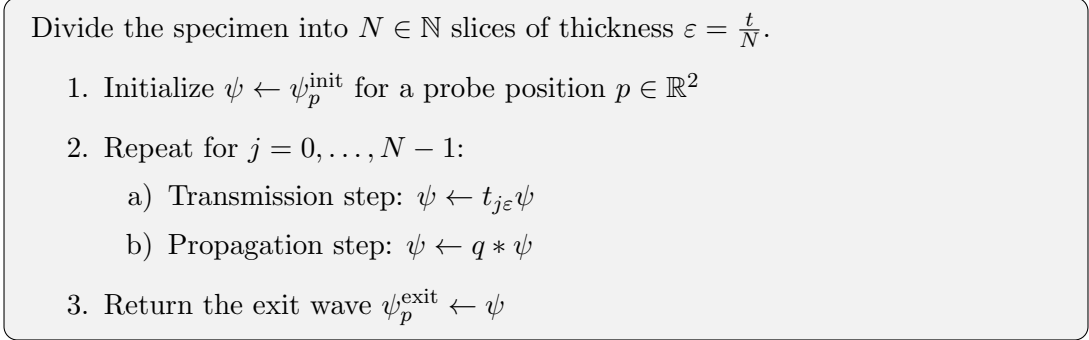


Figure 1: Pseudocode for solving the Schrödinger equation with the Multislice algorithm. The error made for each slice is in  $\mathcal{O}(\varepsilon^2)$  so that the overall error is in  $\mathcal{O}(\varepsilon)$  if  $N \sim \frac{1}{\varepsilon}$ .

**Complexity:** In order to estimate the complexity of the Multislice algorithm, we assume that the electron waves are discretized as complex images on a grid of  $X \times Y$  pixels. The propagation step may either be computed as a convolution in real space or as a pointwise multiplication in Fourier space, using the convolution theorem  $q * \psi = \mathcal{F}^{-1}(\mathcal{F}(q)\mathcal{F}(\psi))$  and the fast Fourier transform. The Fourier transform  $\mathcal{F}(q)$  is a constant and can be precomputed. Performing the Multislice algorithm for a single probe position  $p$  requires approximately

$$T_{\text{Multislice}, XY} = N(2XY + 2XY \log(XY))$$

operations if the propagation step is performed in Fourier space and

$$\tilde{T}_{\text{Multislice}, XY} = N(XY + XYK_1K_2)$$

operations if the propagation step is performed as a convolution in real space, where the propagation function  $q$  is discretized to  $K_1 \times K_2$  pixels.

We remark that it is not always necessary to perform the Multislice computations on the entire simulation domain. Both the Fourier space and the real space variant can be computed on smaller windows adjusted to the extent of the probe wave function. However, caution must be exercised when using the Fourier space variant of the Multislice algorithm because of the periodicity of the DFT. If  $X$  and  $Y$  are chosen sufficiently large, this problem is alleviated by the decay of the STEM probe to zero. A too small value of  $X$  and  $Y$  on the other hand may cause a significant approximation error due to the wrap-around effect of the DFT.

## 4 Approximation of STEM probes

Solving the Schrödinger equation is the computational bottleneck of STEM image simulation. From a purely mathematical point of view, there are two complementary ways to alleviate this problem. On the one hand, one can try to find better ways of solving the Schrödinger equation, which means using a faster or more accurate method than the Multislice algorithm. On the other hand, one can try to reduce the number of times that the Schrödinger equation needs to be solved. In this section, we will be discussing the latter approach.

In the following, the size of the discretized simulation domain in pixels is given by  $X \times Y$  for  $X, Y \in \mathbb{N}$ .

### 4.1 Fourier space approximation in PRISM

The PRISM algorithm [11] is based on one key observation: instead of propagating the STEM probes themselves through the specimen, it is equally possible to first propagate each of their discrete frequencies individually and afterwards reconstruct the STEM probes as linear combinations of their frequencies.

Consider the discretized STEM probes  $\hat{\psi}_p^{\text{init}}$  on a grid of  $X \times Y$  pixels with a total physical dimension of  $l_x \times l_y$  Ångströms, where  $l_x, l_y \in \mathbb{R}$ . According to Equation (2), the Fourier space values  $\mathcal{F}(\hat{\psi}_p^{\text{init}}) \in \mathbb{C}^{X \times Y}$  may be given as

$$\mathcal{F}(\hat{\psi}_p^{\text{init}})_{k_x, k_y} = \exp(-i\chi(g(k_x, k_y)))A(g(k_x, k_y))\mu_{-p}(g(k_x, k_y))$$

for all  $k_x \in \{1, \dots, X\}$ ,  $k_y \in \{1, \dots, Y\}$ , where

$$g(k_x, k_y) = \left( \frac{k_x - 1 - \lfloor X/2 \rfloor}{l_x}, \frac{k_y - 1 - \lfloor Y/2 \rfloor}{l_y} \right)$$

converts pixel coordinates  $(k_x, k_y)$  to the corresponding frequencies. The Fourier transform turns translations in real space coordinates into modulations in Fourier space, where the modulation by  $p \in \mathbb{R}^2$  is defined as

$$\mu_p : \mathbb{R}^2 \rightarrow \mathbb{C}, \quad k \mapsto \exp(2\pi i k \cdot p).$$

The value  $\mathcal{F}(\hat{\psi}_p^{\text{init}})_{k_x, k_y}$  is nonzero if and only if

$$(k_x, k_y) \in \mathcal{K} := \{(k_x, k_y) \in \{1, \dots, X\} \times \{1, \dots, Y\} \mid A(g(k_x, k_y)) \neq 0\}.$$

Expressing  $\mathcal{F}(\hat{\psi}_p^{\text{init}})$  as a linear combination of discrete dirac deltas, it follows that

$$\mathcal{F}(\hat{\psi}_p^{\text{init}}) = \sum_{(k'_x, k'_y) \in \mathcal{K}} \mathcal{F}(\hat{\psi}_p^{\text{init}})_{k'_x, k'_y} \delta_{(k'_x, k'_y)},$$

where  $\delta_b \in \mathbb{R}^{X \times Y}$  with

$$(\delta_b)_a = \begin{cases} 1, & \text{if } a = b, \\ 0, & \text{otherwise} \end{cases}$$

for all  $a, b \in \{1, \dots, X\} \times \{1, \dots, Y\}$ . Consequently, taking the inverse discrete Fourier transform yields

$$\hat{\psi}_p^{\text{init}} = \sum_{(k'_x, k'_y) \in \mathcal{K}} \mathcal{F} \left( \hat{\psi}_p^{\text{init}} \right)_{k'_x, k'_y} \underbrace{\mathcal{F}^{-1} \left( \delta_{(k'_x, k'_y)} \right)}_{=: w_{k'_x, k'_y}}. \quad (6)$$

The plane waves  $w_{k'_x, k'_y}$  are the functions that are transmitted through the specimen in the PRISM algorithm instead of the probes  $\hat{\psi}_p^{\text{init}}$ .

Let  $\mathcal{P} \subseteq \mathbb{R}^2$  be the set of all probe positions that form the final STEM image. If  $W_{k'_x, k'_y}$  denotes the solution to the Schrödinger equation for the initial condition  $w_{k'_x, k'_y}$ , then the exit waves are given by

$$\hat{\psi}_p^{\text{exit}} = \sum_{(k'_x, k'_y) \in \mathcal{K}} \mathcal{F} \left( \hat{\psi}_p^{\text{init}} \right)_{k'_x, k'_y} W_{k'_x, k'_y} \quad (7)$$

for all  $p \in \mathcal{P}$  due to the linearity of the Schrödinger equation.

Although the number of plane waves  $w_{k'_x, k'_y}$  may be much smaller than the number of probe positions  $|\mathcal{P}|$  and the Schrödinger equation only needs to be solved for the plane wave initial conditions, this approach may still be slower than the standard Multislice algorithm for two reasons:

1. Evaluating (7) for every probe position  $p \in \mathcal{P}$  requires a large number of floating point operations and may take a long time depending on the size of  $|\mathcal{K}|$ .
2. All of the  $W_{k'_x, k'_y}$  for  $(k'_x, k'_y) \in \mathcal{K}$  need to be kept in memory at the same time, causing large memory consumption and potentially slow memory access.

To a certain extent, both of these problems are alleviated by the PRISM interpolation factor. This is a factor  $f \in \mathbb{N}$  which reduces the number of plane waves by considering only every  $f$ -th dirac delta in Fourier space. Formally, the set  $\mathcal{K}$  is replaced by

$$\mathcal{K}_f := \mathcal{K} \cap \left( \left( f\mathbb{Z} + 1 + \left\lfloor \frac{X}{2} \right\rfloor \right) \times \left( f\mathbb{Z} + 1 + \left\lfloor \frac{Y}{2} \right\rfloor \right) \right)$$

and the approximation

$$\hat{\psi}_p^{\text{init}} \approx \sum_{(k'_x, k'_y) \in \mathcal{K}_f} \mathcal{F} \left( \hat{\psi}_p^{\text{init}} \right)_{k'_x, k'_y} w_{k'_x, k'_y} \quad (8)$$

leads to

$$\hat{\psi}_p^{\text{exit}} \approx \sum_{(k'_x, k'_y) \in \mathcal{K}_f} \mathcal{F} \left( \hat{\psi}_p^{\text{init}} \right)_{k'_x, k'_y} W_{k'_x, k'_y}. \quad (9)$$

Choose an interpolation factor  $f \in \mathbb{N}$ .

1. For each  $k' \in \mathcal{K}_f$ , use the Multislice algorithm (cf. Figure 1) to calculate the solution  $W_{k'}$  to the Schrödinger equation with initial condition  $w_{k'}$ .
2. For each probe position  $p \in \mathcal{P}$ , calculate an approximation to the corresponding exit wave using Equation (9).

Figure 2: Pseudocode for the PRISM algorithm.

The set  $\mathcal{K}_f$  is depicted in the top row of Figure 3 for  $f \in \{1, 2, 4\}$ . This is an elegant way to speed up the computations and reduces the number of times that the Schrödinger equation needs to be solved by a factor of  $|\mathcal{K}|/|\mathcal{K}_f| \approx f^2$ . The PRISM algorithm is summarized in Figure 2.

A major practical difficulty in this approach is the implicit repetition of the STEM probe in the approximation (8). Using an interpolation factor of  $f \in \mathbb{N}$  causes  $f^2$  evenly spaced STEM probes to appear in the approximation (8), which means that the approximate solution to the Schrödinger equation in (9) corresponds to propagating  $f^2$  copies of the STEM probe through the specimen simultaneously. This effect is depicted in the bottom row of Figure 3.

Consequently, the approximations (8) and (9) are valid only locally near the center  $p$  of the probe and "interference" with nearby artificial copies of the probe may introduce significant numerical errors if  $f$  is too large. For this reason, the approximations (9) are cropped to a window of  $(X/f) \times (Y/f)$  pixels centered at the probe position in the PRISM algorithm, which is both beneficial and detrimental. It is beneficial, because it reduces the number of operations that are necessary to evaluate (9) by  $f^2$ . At the same time, it is detrimental because the useful area of the simulation window is unavoidably reduced by the same factor  $f^2$ .

Overall, the number of necessary floating point operations to compute one STEM image with the PRISM algorithm can be roughly estimated as

$$\begin{aligned} T_{\text{PRISM}} &= |\mathcal{K}_f| T_{\text{Multislice}, XY} + |\mathcal{P}| |\mathcal{K}_f| \frac{XY}{f^2} \\ &\approx \frac{1}{f^2} |\mathcal{K}| N(2XY + 2XY \log(XY)) + \frac{1}{f^4} |\mathcal{P}| |\mathcal{K}| XY. \end{aligned}$$

The first term consists of the number of operations necessary to compute the solutions  $W_k$  to the Schrödinger equation with initial condition  $w_k$  for all  $k \in \mathcal{K}$  and the second term accounts for the evaluation of (9). Thermal diffuse scattering and partial coherence are not included in this formula and would result in multiplying  $T_{\text{PRISM}}$  by the number of frozen phonon passes and probe configurations respectively.

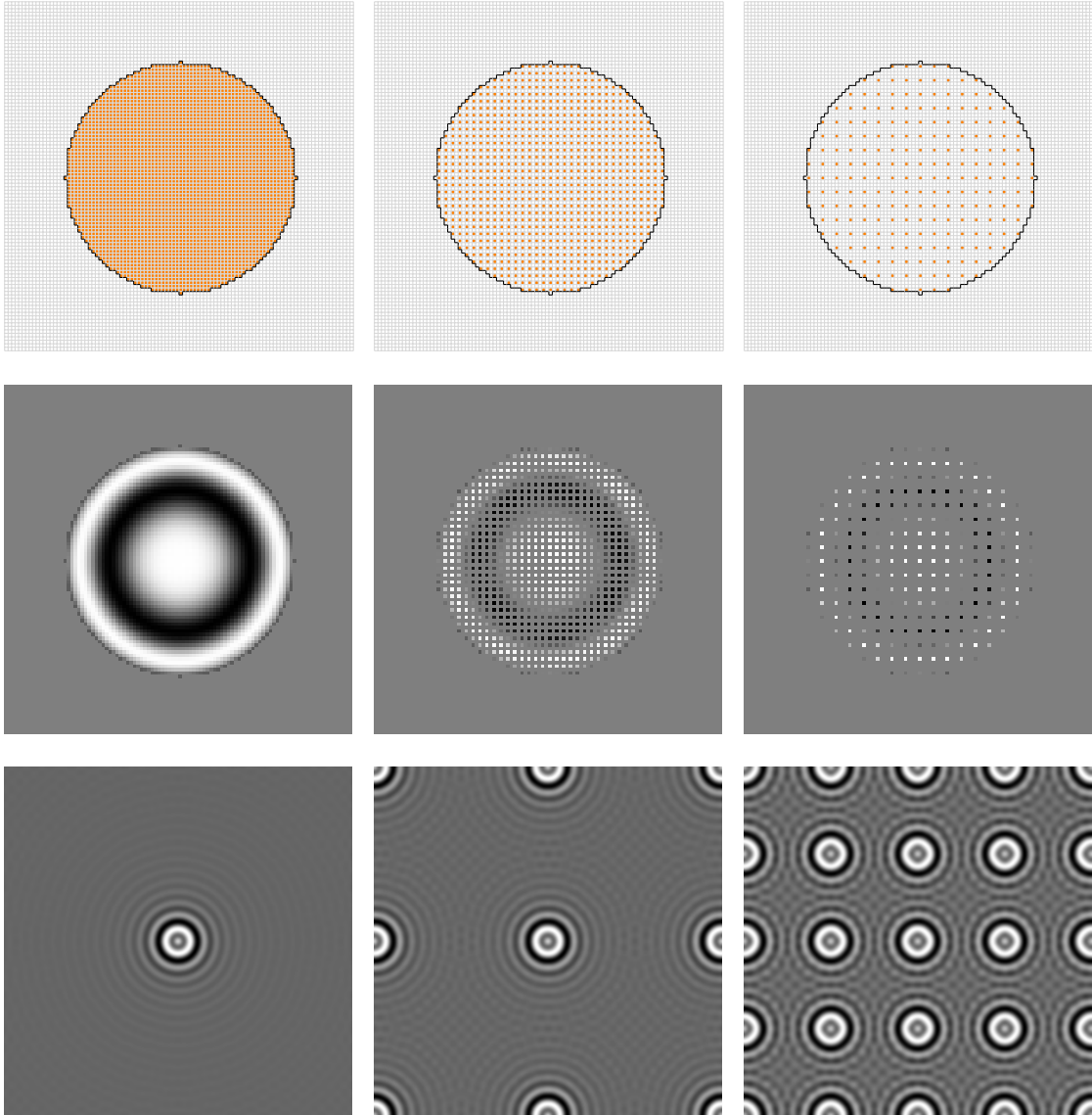


Figure 3: From left to right: the approximation (8) with PRISM interpolation factor  $f = 1$ ,  $f = 2$  and  $f = 4$ . From top to bottom: the elements of the set  $\mathcal{K}_f$  denoted by the filled pixels (top row), the real part of (8) in Fourier space, cropped to a small area around the non-zero frequencies, (middle row) and the real part of (8) in real space (bottom row). Note that the images have periodic boundary conditions due to the periodicity of the discrete Fourier transform.

## 4.2 Real space approximation

Since the implicit probe repetition in the PRISM approximation renders large values of  $f$  unusable, the number of solutions  $W_{k'_x, k'_y}$  that need to be calculated may still be too large to keep all of them in computer memory at the same time. Additionally, all of the plane waves  $w_{k'_x, k'_y}$  have unbounded support in real space coordinates and span the entire specimen area. Thus, if small local changes are made to the specimen in question, all of the solutions  $W_{k'_x, k'_y}$  need to be recomputed.

In order to address these problems, we first take an algebraic point of view on the approximation of the STEM probes. Denote by

$$\mathcal{P} := \left\{ a \begin{pmatrix} p_x \\ 0 \end{pmatrix} + b \begin{pmatrix} 0 \\ p_y \end{pmatrix} \mid a \in \{0, \dots, P_x - 1\}, b \in \{0, \dots, P_y - 1\} \right\}$$

the set of all STEM probe positions that form the final STEM image, where  $P_x, P_y \in \mathbb{N}$  are the number of pixels of the output STEM image and  $p_x, p_y \in \mathbb{R}$  is the spacing in between the pixels. The vector space generated by all probe functions is

$$V_{\mathcal{P}} := \langle \hat{\psi}_p^{\text{init}} \mid p \in \mathcal{P} \rangle_{\mathbb{C}} \subseteq \mathbb{C}^{X \times Y}.$$

By (6), this vector space satisfies

$$V_{\mathcal{P}} \subseteq \langle w_k \mid k \in \mathcal{K} \rangle_{\mathbb{C}}$$

and therefore the dimension of  $V_{\mathcal{P}}$  as a complex vector space is bounded by  $|\mathcal{K}|$ , regardless of the number of probe positions  $|\mathcal{P}|$ . The goal is now to find a new basis for  $V_{\mathcal{P}}$ , which avoids the problems of the plane wave basis  $(w_k)_{k \in \mathcal{K}}$ . This is summarized as follows:

**Task 4.1.** Find a basis  $(u_i)_{i \in \mathcal{I}}$  for a vector space  $U \subseteq \mathbb{C}^{X \times Y}$  with  $V_{\mathcal{P}} \subseteq U$  and dimension  $\dim_{\mathbb{C}}(U) \leq |\mathcal{K}|$  such that the basis elements  $u_i$  have a small support in real space coordinates.

Given such a basis  $(u_i)_{i \in \mathcal{I}}$ , one can first compute solutions to the Schrödinger equation with the initial conditions  $u_i$  and then express the STEM probes  $\hat{\psi}_p^{\text{init}}$  as linear combinations of the basis elements  $(u_i)_{i \in \mathcal{I}}$ . Due to the linearity of the Schrödinger equation, the exit waves  $\hat{\psi}_p^{\text{exit}}$  can subsequently be computed similarly as in PRISM.

The requirement on the basis elements  $u_i$  to have small support in real space is essential and can equivalently be phrased by requiring the  $u_i$  to be localized in real space. Because of this, a position in real space can be assigned to each  $u_i$  in a similar fashion as is naturally done for the STEM probes.

### 4.2.1 The Lattice Multislice Algorithm

We begin by giving a high-level description of a new algorithm for STEM image simulation, which is based on the approximation of STEM probes by elements  $u_i$  as in Task 4.1. The details are then discussed in the subsequent sections. It is pointed out

that the derivation of this algorithm involves some simplifications to facilitate its practical implementation. These simplifications seem natural, but there are likely other approaches that perform equally well or better, although it is unclear to what extent.

We call the rectangular standard lattice that is composed of the probe positions  $\mathcal{P}$  the probe lattice. Due to the regular spacing of the STEM probes, it seems reasonable to choose the functions  $u_i$  to lie on a rectangular standard lattice too, which we call the input wave lattice. The functions  $u_i$  are called input waves in the following. We only consider the case where all  $u_i$  are equal to a shifted version of one common base function  $u$ , just like all STEM probes  $\hat{\psi}_p^{\text{init}}$  are equal up to their position  $p \in \mathcal{P}$ . Without loss of generality, let  $\mathcal{I}$  be the set of input wave positions such that  $u_i = u \circ t_i$  for all  $i \in \mathcal{I}$  with the translation  $t_i : \mathbb{R}^2 \rightarrow \mathbb{R}^2$ ,  $x \mapsto x + i$ . Then

$$\mathcal{I} = \left\{ a \begin{pmatrix} r_x \\ 0 \end{pmatrix} + b \begin{pmatrix} 0 \\ r_y \end{pmatrix} + \mathcal{I}_{\text{offset}} \mid a \in \{0, \dots, R_x - 1\}, b \in \{0, \dots, R_y - 1\} \right\}$$

with the number of input waves  $R_x, R_y \in \mathbb{N}$  for each direction and the spacing  $r_x, r_y \in \mathbb{R}$  as well as an offset  $\mathcal{I}_{\text{offset}} \in \mathbb{R}^2$ , which may also be zero.

Both the probe lattice and the input wave lattice are required to cover the entire simulation domain, respecting its periodicity. If the simulation domain has a physical size of  $l_x \times l_y$  with  $l_x, l_y \in \mathbb{R}$ , then this means that

$$\begin{aligned} P_x p_x - l_x &= P_y p_y - l_y = 0, \\ R_x r_x - l_x - (\mathcal{I}_{\text{offset}})_1 &= R_y r_y - l_y - (\mathcal{I}_{\text{offset}})_2 = 0. \end{aligned} \tag{10}$$

Finally, we also require the probe and input wave lattices to be compatible in the sense that there exist integers  $c, d \geq 1$  such that

$$R_x = cP_x \quad \text{and} \quad R_y = dP_y \tag{Case 1}$$

or

$$P_x = cR_x \quad \text{and} \quad P_y = dR_y. \tag{Case 2}$$

In the first case, the number of input waves is greater than or equal to the number of probe positions,  $|\mathcal{I}| \geq |\mathcal{P}|$ , and in the second case this inequality is reversed. The key restriction here is that the dimensions of one lattice are an integral multiple of the dimensions of the other lattice. While in PRISM the coefficients for the best  $L^2$ -approximation of the STEM probe as linear combinations of the  $w_k$  for  $k \in \mathcal{K}_f$  are given directly by the Fourier space values of the STEM probe (cf. equations [6],[8]), it is not as straightforward to find coefficients to approximate  $\hat{\psi}_p^{\text{init}}$  by a linear combination of the  $u_i$ . In practice, these coefficients can be precomputed with a linear least squares approximation; requiring the lattices to be compatible greatly reduces the computational cost of this precomputation step. This is discussed in more detail in Section 4.2.2.

Although, from a mathematical point of view, the number of elements of  $\mathcal{I}$  can clearly be chosen smaller than or equal to the number of probe positions  $|\mathcal{P}|$  for a good approximation of the STEM probes, it is not clear that this is always beneficial for the

computations (see Section 4.2.3 for a discussion of some possible input waves). Therefore, we don't exclude the case  $|\mathcal{I}| > |\mathcal{P}|$ . The probe and input wave lattices are schematically depicted in Figure 4.

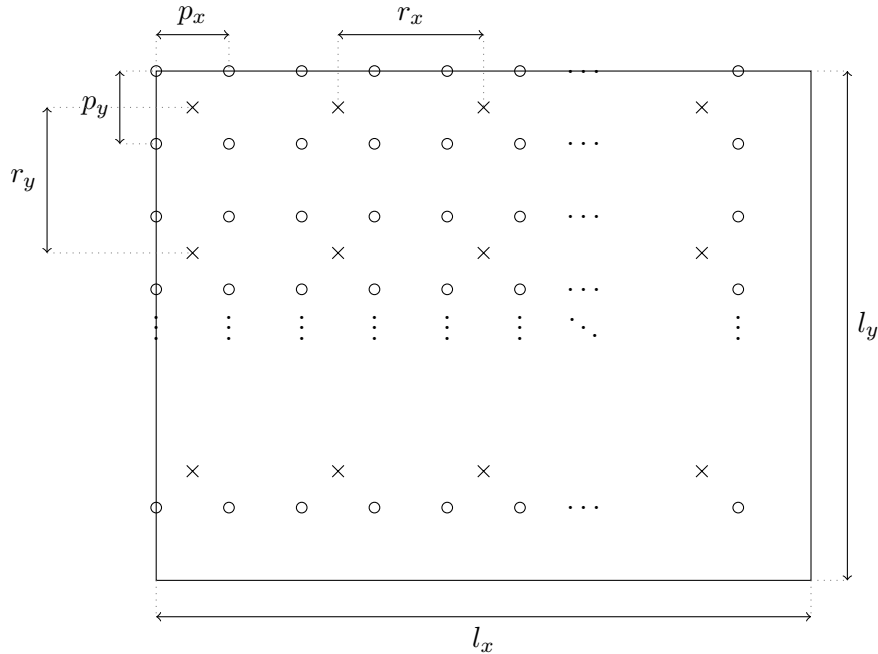


Figure 4: Exemplary sketch of the probe and input wave lattices drawn on top of the simulation domain. The probe positions  $\mathcal{P}$  are denoted by circles and the input wave positions  $\mathcal{I}$  by crosses. In this case, we have  $P_x = 2R_x$  and  $P_y = 2R_y$  as well as  $\mathcal{I}_{\text{offset}} = (p_x/2, p_y/2)$ . Note the compatibility of both lattices and that they cover the entire specimen domain, respecting the periodic boundaries.

If we used a full real space basis  $(u_i)_{i \in \mathcal{I}}$  as in Task 4.1 for the approximation of the STEM probes, then at most a minor improvement of the computation time compared to the standard Multisllice algorithm is expected. In PRISM, the computational speed up is achieved by reducing the number of basis elements from  $|\mathcal{K}|$  to  $|\mathcal{K}_f|$ , which accordingly reduces the number of times that the Schrödinger equation needs to be solved. It is possible to trade off computation time against accuracy in a similar way when working with localized real space functions  $u_i$ . Among all the possibilities to do so, we note in particular the following three approaches:

- (i) Considering only every  $f$ -th point on the input wave lattice in both directions, thereby reducing the number of evaluations of the Multisllice algorithm by a factor of  $f^2$ .
- (ii) Performing the Multisllice algorithm on a smaller computation window of the size

$X' \times Y'$  for  $X', Y' \in \mathbb{N}$  with  $X' < X$ ,  $Y' < Y$ , adjusted to the extent of the localized real space functions  $u_i$ .

- (iii) For a STEM probe  $\hat{\psi}_p^{\text{init}}$ , considering only the  $L \in \mathbb{N}$  input waves  $u_i$  closest to the probe position  $p$  for the approximation of  $\hat{\psi}_p^{\text{init}}$ .

The first option (i) is very similar to PRISM's interpolation factor. The set of the input wave positions attained by only considering every  $f$ -th point of the input wave lattice is denoted by

$$\mathcal{I}_f := \left\{ af \begin{pmatrix} r_x \\ 0 \end{pmatrix} + bf \begin{pmatrix} 0 \\ r_y \end{pmatrix} + \mathcal{I}_{\text{offset}} \mid a \in \{0, \dots, R_x/f - 1\}, b \in \{0, \dots, R_y/f - 1\} \right\},$$

where we generally assume that  $R_x$  and  $R_y$  are multiples of  $f$  by rounding up to the next multiple of  $f$  if necessary and adjusting the probe lattice accordingly. Option (ii) is analogous to the approach of reducing the size of the computation window by a factor of  $f^2$ ; the only difference here is, that solutions to the Schrödinger equation are computed for the input waves as initial condition instead of the STEM probes. The third option (iii) is unique to this approach and only possible because both the STEM probes and the input waves are localized in real space. It is motivated by the idea that input waves close to the center of a STEM probe may contribute more to its approximation than those further away. The parameter  $L$  can be freely chosen to adjust the number of input waves that are considered for the approximation of a given STEM probe.

It should be noted that (i) and (iii) are not independent from each other. A larger value of  $f$  generally requires a larger value of  $L$  to achieve the same approximation quality and vice versa. The second option (ii) is mostly interesting in the case where the Multislice algorithm is entirely performed in real space without use of the Fourier transform, as the periodicity of the DFT likely does not match the periodicity of the specimen for computation windows smaller than whole simulation domain. Nonetheless, if  $U_i$  denotes the solution to the Schrödinger equation with initial condition  $u_i$ , then  $U_i$  will also be fairly well localized in real space. This means that the result can always be cropped to a smaller computation domain, which can save large amounts of computer memory. While (i) is the main factor for reducing the computation times, (iii) also plays an important role as can be seen in the expressions for the computational complexity below.

All that has been described above leads to a new algorithm for the simulation of STEM images, which is summarized in Figure 5. This algorithm is referred to as the Lattice Multislice Algorithm (LMA) due to the important role of the probe and input wave lattices.

The exact formula for calculating the linear combination in the second step in Figure 5 is given in Section 4.2.2.

**Computational complexity** We keep the same notation as before, where the simulation domain is discretized to  $X \times Y$  pixel, and denote by  $X' \times Y'$  the size of the smaller

Initialization: choose a localized real space function  $u$ , the input wave lattice  $\mathcal{I}$  as well as  $f \in \mathbb{N}$  and  $L \in \mathbb{N}$ . Precompute the approximation coefficients.

1. For each  $i \in \mathcal{I}_f$ , use the Multislice algorithm (cf. Figure 1) to calculate the solution  $U_i$  to the Schrödinger equation with initial condition  $u_i$ .
2. For each probe position  $p \in \mathcal{P}$ , calculate an approximation to the corresponding exit wave  $\hat{\psi}_p^{\text{exit}}$  as a linear combination of the  $U_i$  using the precomputed approximation coefficients.

Figure 5: Pseudocode for the Lattice Multislice Algorithm.

computation domain for the input waves in pixel. Disregarding the precomputation of the approximation coefficients, the number of necessary floating point operations to compute one STEM image with the Lattice Multislice Algorithm can be estimated as

$$\begin{aligned} T_{\text{LMA}} &= |\mathcal{I}_f| T_{\text{Multislice}, XY} + |\mathcal{P}| LX'Y' \\ &= \frac{1}{f^2} |\mathcal{I}| N(2XY + 2XY \log(XY)) + |\mathcal{P}| LX'Y' \end{aligned}$$

if the propagation step in the Multislice algorithm is performed in Fourier space using the FFT, or as

$$\begin{aligned} \tilde{T}_{\text{LMA}} &= |\mathcal{I}_f| \tilde{T}_{\text{Multislice}, X'Y'} + |\mathcal{P}| LX'Y' \\ &= \frac{1}{f^2} |\mathcal{I}| N(X'Y' + X'Y' K_1 K_2) + |\mathcal{P}| LX'Y'. \end{aligned}$$

if the propagation step is performed as a convolution in real space.

If we found a basis  $\mathcal{I}$  with  $|\mathcal{K}|$  elements, chose  $L = |\mathcal{K}|/f^2$  and reduced the computation domain to the same size as in PRISM, i.e.  $X' = X/f$  and  $Y' = Y/f$ , then

$$\begin{aligned} T_{\text{LMA}} &= \frac{1}{f^2} |\mathcal{K}| N(2XY + 2XY \log(XY)) + |\mathcal{P}| \frac{|\mathcal{K}|}{f^2} \frac{X}{f} \frac{Y}{f} \\ &= \frac{1}{f^2} |\mathcal{K}| N(2XY + 2XY \log(XY)) + \frac{1}{f^4} |\mathcal{P}| |\mathcal{K}| XY \\ &\approx T_{\text{PRISM}}. \end{aligned}$$

It is interesting to note that if we choose  $X' = X/f$  and  $Y' = Y/f$ , then the first

summand of  $\tilde{T}_{\text{LMA}}$  is proportional to  $f^{-4}$ . Comparing this to  $T_{\text{LMA}}$  yields

$$\begin{aligned}
& \tilde{T}_{\text{LMA}} \leq T_{\text{LMA}} \\
\iff & \frac{1}{f^2} |\mathcal{I}| N(X'Y' + X'Y'K_1K_2) \leq \frac{1}{f^2} |\mathcal{I}| N(2XY + 2XY \log(XY)) \\
\iff & \frac{1}{f^4} |\mathcal{I}| N(XY + XYK_1K_2) \leq \frac{1}{f^2} |\mathcal{I}| N(2XY + 2XY \log(XY)) \\
\iff & \frac{XY + XYK_1K_2}{2XY + 2XY \log(XY)} \leq f^2 \\
\iff & \sqrt{\frac{1}{2} \frac{1 + K_1K_2}{1 + \log(XY)}} \leq f,
\end{aligned}$$

or, approximately,

$$f \gtrsim \sqrt{\frac{K_1K_2}{2 \log(XY)}}.$$

For a simulation domain size of  $2048^2$  pixels and a discretized convolution kernel with a width and height of 25 pixels, the above inequality is true if and only if  $f \geq 4$ .

#### 4.2.2 Approximation coefficients

In principle, it is possible to calculate approximation coefficients  $\alpha_{p,i} \in \mathbb{C}$  for all probe positions  $p \in \mathcal{P}$  and all  $i \in \mathcal{I}_f$  such that

$$\hat{\psi}_p^{\text{init}} \approx \sum_{i \in \mathcal{I}_f} \alpha_{p,i} u_i$$

for all  $p \in \mathcal{P}$  using linear least squares. However, this would be a waste of computations due to the compatibility property of the probe and input wave lattices, which makes it possible to reuse the same approximation coefficients for many probe positions. To show how the coefficients can be reused, we distinguish (Case 1) with  $|\mathcal{I}| \geq |\mathcal{P}|$  and (Case 2) with  $|\mathcal{P}| \geq |\mathcal{I}|$ . Both cases are illustrated in Figure 6 and described below.

Denote by  $\mathcal{I}_{f,p,L}$  for  $p \in \mathcal{P}$  the subset of  $\mathcal{I}_f$  containing the  $L$  closest input waves to  $p$ . Looking at (Case 1) in more detail, it is easy to see that only the coefficients for the approximation of a single probe need to be calculated and can in turn be reused for all other probe positions. Explicitly, if

$$\hat{\psi}_0^{\text{init}} \approx \sum_{i \in \mathcal{I}_{f,0,L}} \alpha_i u_i \quad (11)$$

for suitable  $\alpha_i \in \mathbb{C}$ , then

$$\hat{\psi}_p^{\text{init}} \approx \sum_{i \in \mathcal{I}_{f,0,L}} \alpha_i u_{i+p}. \quad (12)$$

with precisely the same approximation error for all  $p \in \mathcal{P}$ . Here,  $i + p$  is understood to be calculated in  $\mathbb{R}^2 / (l_x \mathbb{Z} \times l_y \mathbb{Z})$  and again an element of  $\mathcal{I}_f$  due to the compatibility of the lattices and (10).

For (Case 2), in total  $c \cdot d$  unique sets of coefficients need to be calculated for the probe positions in

$$\mathcal{P}_{\text{approx}} := \left\{ a \begin{pmatrix} p_x \\ 0 \end{pmatrix} + b \begin{pmatrix} 0 \\ p_y \end{pmatrix} \mid a \in \{0, \dots, c-1\}, b \in \{0, \dots, d-1\} \right\}.$$

If the approximations are given by

$$\hat{\psi}_p^{\text{init}} \approx \sum_{i \in \mathcal{I}_{f,p,L}} \alpha_{p,i} u_i \quad \forall p \in \mathcal{P}_{\text{approx}} \quad (13)$$

for suitable  $\alpha_{p,i} \in \mathbb{C}$ , then, similarly to Equation (12),

$$\hat{\psi}_{p+q}^{\text{init}} \approx \sum_{i \in \mathcal{I}_{f,p,L}} \alpha_{p,i} u_{i+q} \quad \forall p \in \mathcal{P}_{\text{approx}} \quad (14)$$

holds for all  $q = xcp_x e_1 + ydp_y e_2$  with  $x, y \in \mathbb{N}$  such that  $p+q \in \mathcal{P}$ , where  $e_1 = (1 \ 0)$  and  $e_2 = (0 \ 1)$ . As above,  $i+q$  is understood to be calculated as an element of  $\mathbb{R}^2 / (l_x \mathbb{Z} \times l_y \mathbb{Z})$  and again contained in  $\mathcal{I}_f$ .

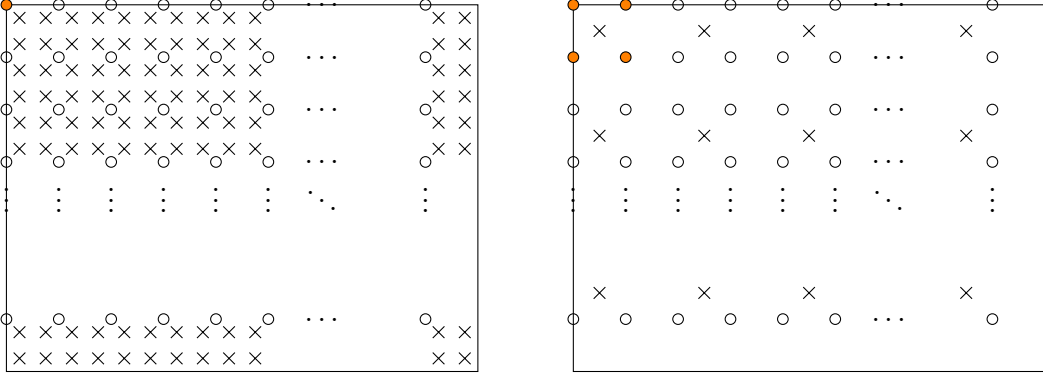


Figure 6: Example for (Case 1) on the left and (Case 2) on the right. Circles indicate probe positions and crosses indicate input wave positions in  $\mathcal{I}_f$  drawn on top of the simulation domain depicted by the large rectangle. The probe positions with unique sets of coefficients as in Equations (11) and (13) are denoted by the filled circles. For the sake of simplicity, we disregard rotational and mirror symmetries in the coefficients, which would reduce the required amount of precomputations even further.

### 4.2.3 Input wave functions

The description of the Lattice Multislice Algorithm is incomplete without a discussion of possible choices for the input waves. By definition, the STEM probes  $\hat{\psi}_p^{\text{init}}$  form a generating system for  $V_{\mathcal{P}}$ , so an obvious choice is  $u = \hat{\psi}_0^{\text{init}}$ . This is an interesting choice because it makes the approximation very easy by requiring only comparatively small

values of  $L$  as is shown below. If we additionally choose  $\mathcal{I} = \mathcal{P}$ ,  $f = 1$  and  $L = 1$ , then we retrieve the standard algorithm for the simulation of STEM images, where the Schrödinger equation is solved once for every probe position with the STEM probes itself as initial conditions.

A more interesting case arises if we deviate from these parameters, in particular if we increase  $f$  (and, necessarily,  $L$ ). In order to avoid a large spread in the approximation errors for different probe positions, we choose the input wave lattice to be identical to the probe lattice, but shifted by half of the probe spacing  $p_x/2$  and  $p_y/2$  in each direction respectively. Explicitly, we set  $\mathcal{I} := \mathcal{P} + \frac{1}{2}(p_x, p_y)$ . Without this shift, the approximation would be perfect for every probe position  $p \in \mathcal{P} \cap \mathcal{I}_f$ , but subject to an error for all probe positions  $p \in \mathcal{P} \setminus \mathcal{I}_f$ . This may cause potentially significant artifacts in a checkerboard pattern in the simulated STEM image for  $f > 1$ .

An example of the magnitude of the approximation error for one particular kind of parameters for  $u = \hat{\psi}_0^{\text{init}}$  is shown in Figure 7 for varying values of  $f$  and  $L$ . When increasing  $L$ , the approximation error generally appears to decrease in a staircase fashion: increasing  $L$  by 1 either results in a minimal or a very large reduction of the approximation error.

Input waves with smaller support or faster decay to zero in real space than the STEM probes require less computer memory and accelerate the computations if the propagation step in the Multislice algorithm is performed as a convolution in real space. However, input waves with a smaller support will in general require larger values of  $L$  or smaller values of  $f$  in order to achieve the same approximation error as other input waves with larger values of  $f$  or smaller  $L$ . This in turn increases the required computer memory and computation time. It is unclear what the optimal choice of  $u$  is, both with respect to the use of computer memory and computation time.

We present a few nontrivial choices of input waves in the following, alongside with numerical experiments depicting the tradeoff of smaller support vs. the choice of  $L$  and  $f$  and the resulting approximation errors.

**Trigonometric polynomials** The trigonometric polynomials introduced in [12] are an attractive choice for the input waves due to their property of being optimally localized in real space for a given degree. They may be extended to a two-dimensional function in several ways. One option is to define  $u$  as the tensor product  $u(x, y) := \varphi_n(x)\varphi_n(y)$ , where

$$\varphi_n(t) = \sum_{k=-n}^n e^{ikt} \cos\left(\frac{k\pi}{2n+2}\right) \quad \forall t \in \mathbb{R}$$

is the trigonometric polynomial of degree  $n \in \mathbb{N}$  defined in [12]. This option has the advantage that the approximation coefficients can be computed directly from the formulas for the frequencies of the trigonometric polynomials and the STEM probes, not necessitating a least squares approximation. Another option is to define  $u$  as the circularly symmetric function given by  $u(v) := \varphi_n(\|v\|_2)$ . The degree  $n$  of  $\varphi_n$  determines its maximum frequency and can be calculated from the maximum frequency of the STEM

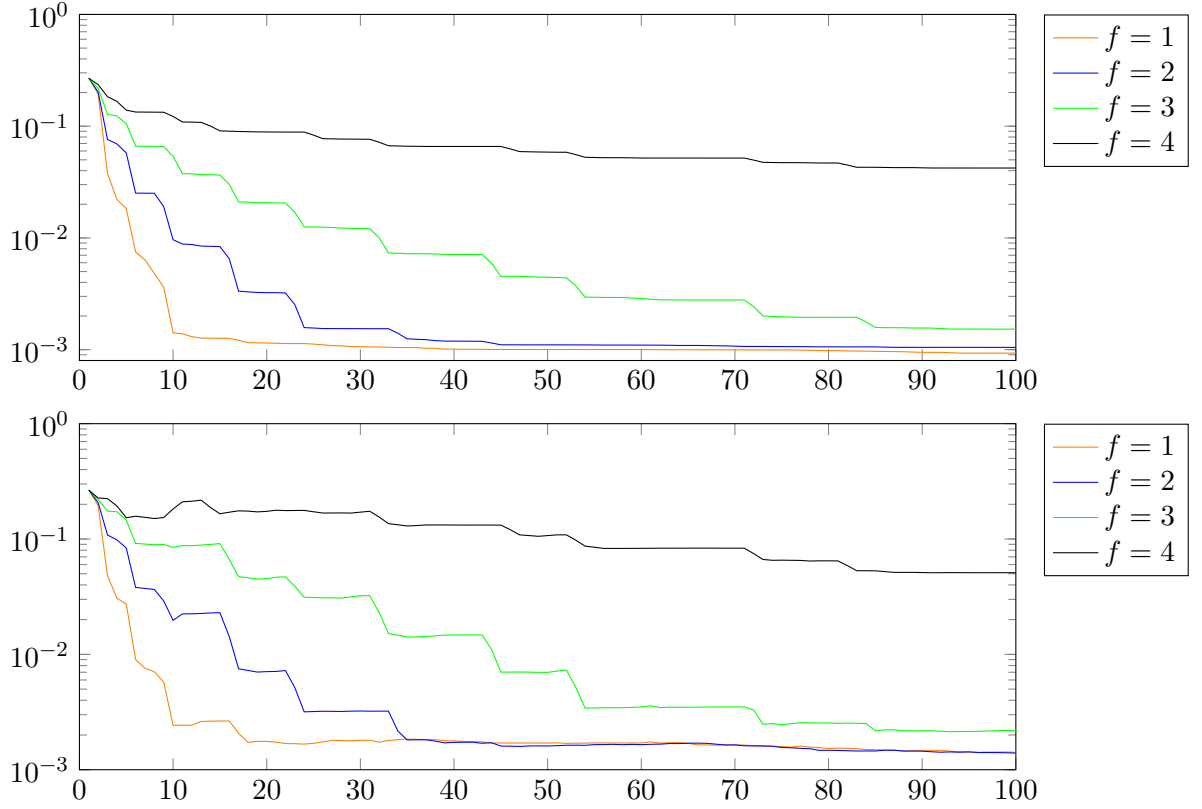


Figure 7: Relative approximation errors for the approximation of the STEM probe  $\hat{\psi}_0^{\text{init}}$  in the euclidean norm (top) and the supremum norm (bottom) for various values of  $f$  and  $L$ . The x axis depicts the value of  $L$  and the y axis the approximation error. The approximations have been computed with linear least squares. The parameters used are  $u = \hat{\psi}_0^{\text{init}}$  and  $\mathcal{I} = \mathcal{P} + \frac{1}{2}(p_x, p_y)$  with  $X = Y = 1024$  and  $P_x = P_y = 524$ . The simulation window size is  $l_x = l_y = 62.416$  (in Angstrom) and the microscope settings are  $\lambda = 0.0250793$  (corresponding to an accelerating voltage of  $U = 200000$  Volt),  $Z = 100$ ,  $C_s = -2000$  and  $\alpha_{\text{max}} = 0.026$ .

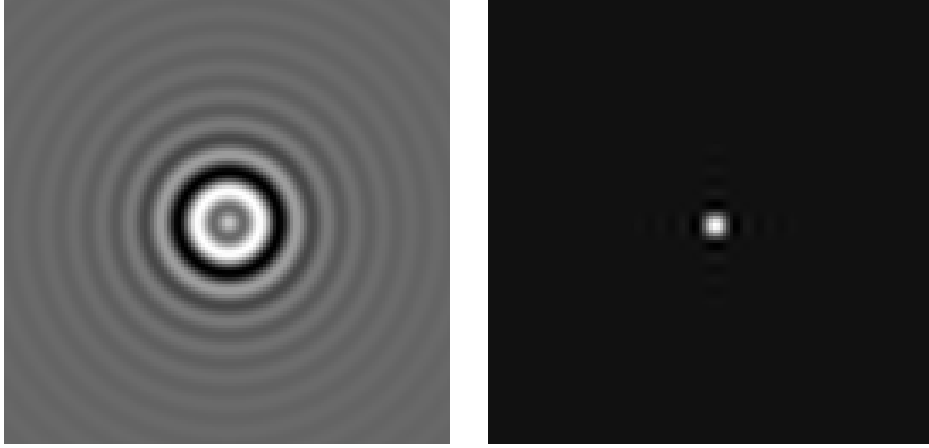


Figure 8: The real part of the STEM probe in real space (left) and the input wave  $u(x, y) := \varphi_n(x)\varphi_n(y)$  with  $n = 7$ . Both images are discretized to  $131 \times 131$  pixels with a pixel size of  $0.1219062 \times 0.1219062$  (in Angstrom) and cover a similar frequency range. The parameters used for the computation of the STEM probe are  $\lambda = 0.0250793$ ,  $Z = 100$ ,  $C_s = -2000$  and  $\alpha_{\max} = 0.026$ .

probes and the Fourier space pixel size  $q \in \mathbb{R}$  as

$$n = \frac{\alpha_{\max}}{\lambda} \cdot \frac{1}{q}.$$

This way, the frequency range of the input waves matches the frequency range of the STEM probes optimally, ensuring a good approximation without wasting computations on unneeded frequencies.

Figure 8 shows an image of a STEM probe next to the tensor product of a trigonometric polynomial as described above with a matching frequency range. Since this type of input wave is much better localized in real space than the probe, it is important to carefully choose the probe and input wave lattices as well as  $f$  such the number of input waves close to a probe position is neither too small nor too large. If the number is too small, then the input waves are spaced too far apart, resulting in a bad approximation. If the number is too large, computation time is wasted. Another helpful perspective is provided by the Fourier space representation: after discretization, the STEM probes are composed of  $N \in \mathbb{N}$  discrete frequencies within the aperture radius. The probe lattice and input wave lattice as well as  $f$  should be chosen such that the number of input waves is close to  $N$  within the area around the probe where the approximation is calculated.

The consequences of this effect can be seen in Figure 9, where the optimal spacing in between the input waves is achieved for  $f = 2$ . This also shows that simply choosing the  $L \in \mathbb{N}$  input waves closest to the probe position as described in Item (iii) in Section 4.2.1 may yield bad approximation results. However, it is unclear how a better subset of the input waves for a given configuration of probe lattice, input wave lattice and input wave type can be found.

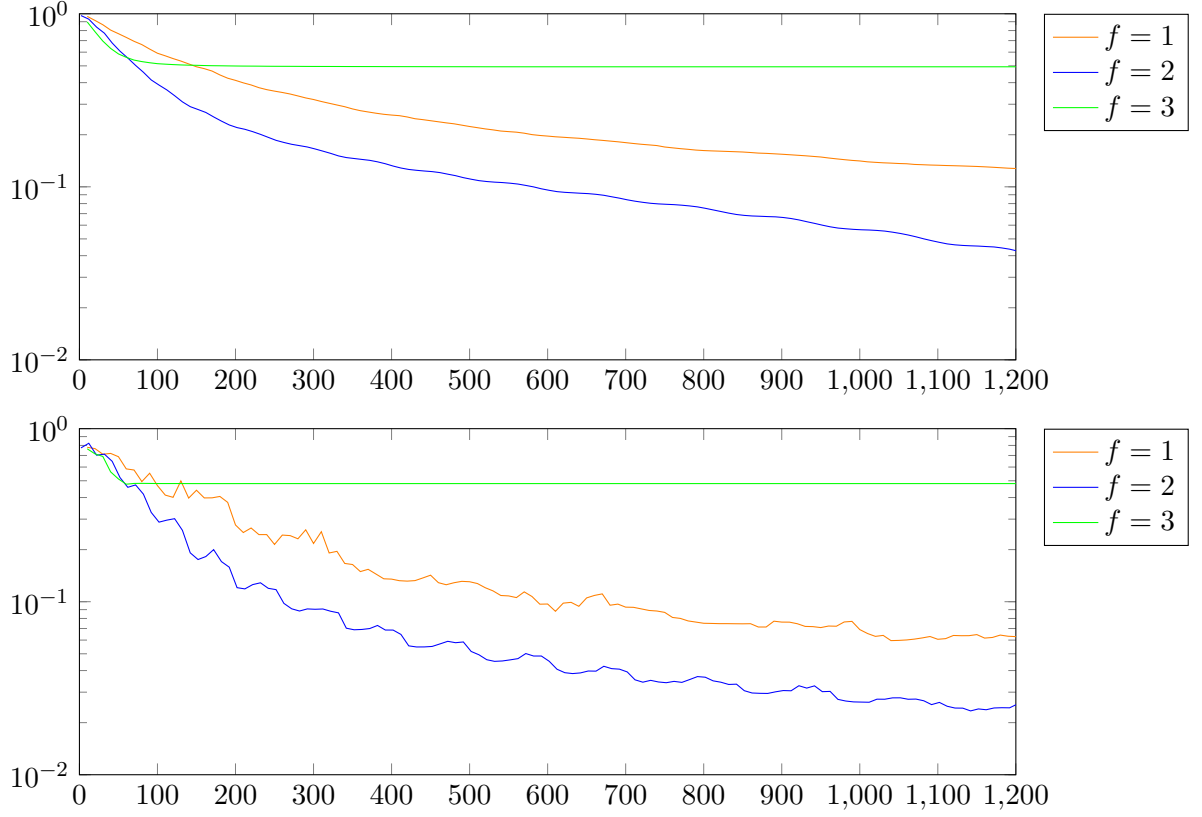


Figure 9: Relative approximation errors for the approximation of the STEM probe  $\hat{\psi}_0^{\text{init}}$  in the euclidean norm (top) and the supremum norm (bottom) for various values of  $f$  and  $L$ . The x axis depicts the value of  $L$  and the y axis the approximation error. The approximations have been computed with linear least squares. The parameters used are  $u(x, y) = \varphi_n(x)\varphi_n(y)$  with  $n = 7$  and  $\mathcal{I} = \mathcal{P} + \frac{1}{2}(p_x, p_y)$  with  $X = Y = 1024$  and  $P_x = P_y = 314$ . The simulation window size is  $l_x = l_y = 62.416$  (in Angstrom) and the microscope settings are  $\lambda = 0.0250793$  (corresponding to an accelerating voltage of  $U = 200000$  Volt),  $Z = 100$ ,  $C_s = -2000$  and  $\alpha_{\text{max}} = 0.026$ .

**Gaussians** When looking for localized functions in real space, it is natural to consider Gaussians

$$g_\sigma(x) := \exp\left(\frac{-\|x\|_2^2}{2\sigma^2}\right) \quad \forall x \in \mathbb{R}^2$$

with variance  $\sigma > 0$ . Although technically non-zero everywhere, in practical computations they can be considered equal to zero sufficiently far away from their center. Gaussians have the useful property that their Fourier transform is again a Gaussian; similarly to the trigonometric polynomials, this makes it possible to choose a reasonable value for the variance based on the frequency range of the STEM probes, for example

$$\sigma = \frac{\lambda}{2\alpha_{\max}}.$$

The approximation results for various values of  $f$  and  $L$  are plotted in Figure 10.

**Pixel input wave** The fact that practically any function can be chosen as an input wave makes the Lattice Multislice Algorithm highly versatile: the STEM probes themselves, trigonometric polynomials, Gaussians, indicator functions of any set and other functions can be chosen as input waves. Since it is difficult to pinpoint the optimal choice of input waves for given STEM probe parameters and given targets such as minimal memory consumption or computation time, it is interesting to look at the extreme cases. Two of these were already discussed: (1) using the STEM probes themselves as input waves with matching probe and input wave lattices  $\mathcal{I} = \mathcal{P}$  with  $f = 1$  and  $L = 1$  and (2) using Fourier space Dirac deltas as input waves as PRISM does. In the first case, we retrieve the original algorithm for STEM image simulation where no approximation as in PRISM or LMA. The second case corresponds to input waves that are optimally localized in Fourier space for a given discretization.

It is equally possible to consider Dirac deltas in real space as input waves, which then correspond to optimally localized input waves in real space for a given discretization. This makes it possible to perform the Multislice computations on a small subset of the simulation window, reducing the amount of computations for every individual Multislice computation. However, this type of input wave requires one input wave for every pixel in the simulation window. Although it is trivial to form the STEM probes from linear combinations of their pixel values and this results in a perfect approximation, this type of input wave is impractical because of the sheer number of necessary Multislice computations and summands in the linear combinations.

**Probe approximation error and error in the output image** In Figure 11, the error in the approximation of the STEM probe by a linear combination of trigonometric polynomial input waves is compared to the error in the final output image for the M1 specimen [4, 1] provided by Douglas Blom at University of South Carolina. Even for a relatively large relative error of – for example – 20% in the probe approximation, the relative euclidean error of the simulated STEM image is substantially smaller than 20% for the simulated BF, ADF and HAADF 2D STEM images as well as 3D STEM. Relative errors

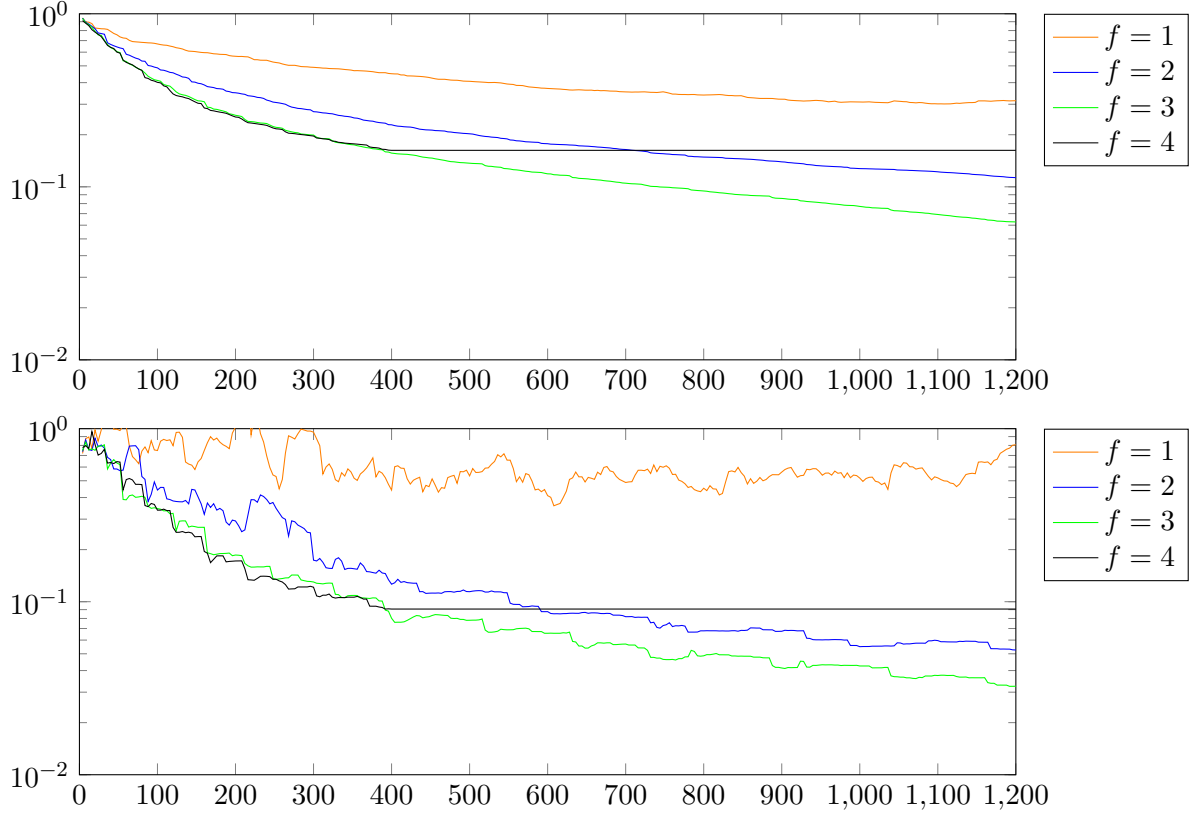


Figure 10: Relative approximation errors for the approximation of the STEM probe  $\hat{\psi}_0^{\text{init}}$  in the euclidean norm (top) and the supremum norm (bottom) for various values of  $f$  and  $L$ . The x axis depicts the value of  $L$  and the y axis the approximation error. The approximations have been computed with linear least squares. The parameters used are  $u = g_\sigma$  with  $\sigma = 0.482$  Angstrom and  $\mathcal{I} = \mathcal{P} + \frac{1}{2}(p_x, p_y)$  with  $X = Y = 1024$  and  $P_x = P_y = 314$ . The simulation window size is  $l_x = l_y = 62.416$  (in Angstrom) and the microscope settings are  $\lambda = 0.0250793$  (corresponding to an accelerating voltage of  $U = 200000$  Volt),  $Z = 100$ ,  $C_s = -2000$  and  $\alpha_{\text{max}} = 0.026$ .

measured in the supremum norm tend to be larger than relative errors in the euclidean norm, but are still below 10% for the BF and HAADF modes in this example.

#### 4.2.4 Partition of the STEM image

Recall that each STEM probe position corresponds to a pixel in the final output image and that the solution to the Schrödinger equation for a STEM probe is approximated by a linear combination of the corresponding solutions for the input waves using the coefficients from Equation (12) or Equation (14). In this section, we assume that the probe and input wave lattices, the simulation window pixel size, the approximation parameters  $f$  and  $L$  as well as the input wave type have been chosen and that the approximation coefficients have been calculated.

One of the main differences of LMA and PRISM is that in LMA each STEM probe is approximated by a different subset of all input waves, whereas in PRISM all input waves are used for the approximation of every STEM probe. Since only a subset of  $L$  input waves is needed at a time, it is possible to calculate Multislice solutions for the input waves only when needed and to discard solutions that are not needed anymore. The memory consumption and computation time can then be adjusted by choosing a suitable order in which the output image pixels are computed.

The most straightforward approach minimizes the computation time: first, compute Multislice solutions for all input wave positions  $\mathcal{I}_f$ ; second, compute all linear combinations to calculate the output image pixels. This requires storing  $|\mathcal{I}_f|$  images (one Multislice solution for each input wave) and  $|\mathcal{I}_f|$  executions of the Multislice algorithm. A strategy that minimizes memory usage is to keep only those  $L$  Multislice solutions in memory that are required to form the linear combinations for the current pixel, discarding solutions that are not needed anymore when continuing with the next pixel. This requires storing only  $L$  images and  $k \in \mathbb{N}$  executions of the Multislice algorithm, where  $|\mathcal{I}_f| \leq k \leq |\mathcal{I}_f| L$ . In general, much less than  $|\mathcal{I}_f| L$  executions will be necessary if the output image pixels are computed in a sensible order. In LMA, the two sets of input wave positions used for the approximation of neighboring probes generally have a large intersection due to the fact that the  $L$  input waves closest to the probe position are chosen for the approximation (cf. Item (iii) on Page 15).

Denote by  $M \in \mathbb{N}$  the maximum number of Multislice solutions for the input waves that can be kept in memory and assume that  $M \geq L$ . If  $M$  is smaller than  $|\mathcal{I}_f|$ , it is necessary to determine an order in which the pixels of the output image are computed, where different orders may require very different overall computation times. We again denote by  $\mathcal{I}_{f,p,L}$  the  $L$  input wave positions in  $\mathcal{I}_f$  closest to a probe position  $p \in \mathcal{P}$ , where  $f \in \mathbb{N}$  is fixed, and extend the notation to all subsets  $S \subseteq \mathcal{P}$  by defining

$$\mathcal{I}_{f,S,L} := \bigcup_{p \in S} \mathcal{I}_{f,p,L}.$$

The idea is now to partition the set of the pixels  $\mathcal{P}$  of the STEM image into subsets  $P_1, \dots, P_l$  such that the number of Multislice solutions required for the computation of all pixels in a set  $P_j$  satisfies  $|\mathcal{I}_{f,P_j,L}| \leq M$  for all  $j = 1, \dots, l$ . If the pixels in  $P_1$  are

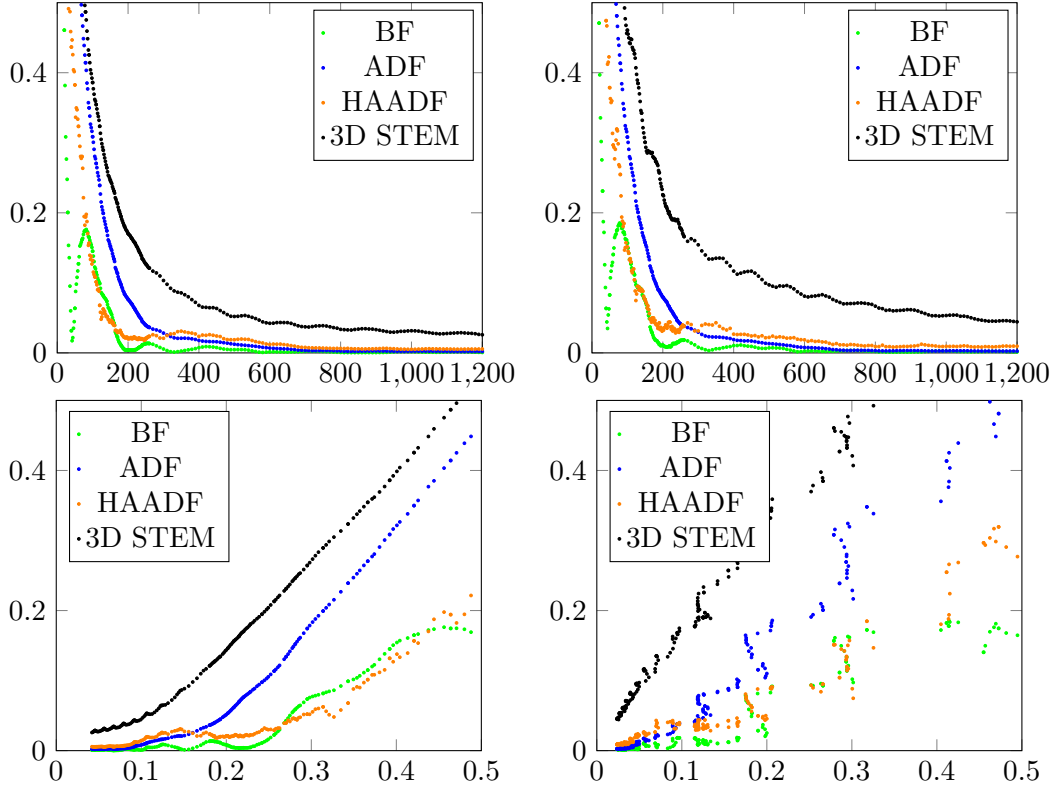


Figure 11: Relative error of the final STEM image of the M1 specimen [4, 1] calculated with LMA as compared to the result from the standard Multislice algorithm for STEM image simulation. Top row: relative error of the final STEM image for different values of  $L$ . Bottom row: relative error of the final STEM image in terms of the relative errors in the approximation of the STEM probes by linear combinations of the input waves. The relative errors are given in the euclidean norm (left column) and in the supremum norm (right column). The parameters are  $u(x, y) = \varphi_n(x)\varphi_n(y)$  with  $n = 7$  and  $(P_x, P_y) = (424, 400)$  with  $X = Y = 1024$ . The input wave lattice  $\mathcal{I}_f$  is chosen as  $\mathcal{I} = \mathcal{P} + \frac{1}{2}(p_x, p_y)$  with  $f = 2$ . The simulation window size is given by  $(l_x, l_y) = (84.54, 79.94)$  (in Angstrom) and the microscope settings are  $\lambda = 0.0250793$  (corresponding to an accelerating voltage of  $U = 200000$  Volt),  $Z = 100$ ,  $C_s = -2000$  and  $\alpha_{\max} = 0.026$ . In order to reduce the computation time, only a  $9 \times 9$  pixel subsection of the final STEM image of size  $P_x \times P_y$  was computed with a single frozen phonon iteration. This is because every data point in the above graphs corresponds to one full STEM image simulation. The integration domains used for the three different 2D STEM images are  $[r_1, r_2] = [0, 15]$  (bright field, BF),  $[r_1, r_2] = [16, 40]$  (annular dark field, ADF) and  $[r_1, r_2] = [41, 200]$  (high angle annular dark field, HAADF) in mrad; cf. Step 3 in Section 3.1.

calculated first, then  $P_2$ ,  $P_3$  and so on, the total number of executions of the Multislice algorithm is

$$T_{P_1, \dots, P_l} := \sum_{j=1}^l |\mathcal{I}_{f, P_j, L}| - \sum_{j=1}^{l-1} |\mathcal{I}_{f, P_j, L} \cap \mathcal{I}_{f, P_{j+1}, L}|.$$

The first sum gives the total number of Multislice solutions required by all of the sets  $P_1, \dots, P_l$  independently of each other and the second sum corresponds to those Multislice solutions needed for the computation  $P_j$  that can be reused for  $P_{j+1}$  and thus do not need to be recomputed.

Identifying a pixel  $a(p_x \ 0) + b(0 \ p_y) \in \mathcal{P}$  by its index  $(a, b)$ , we propose three strategies to compute the Partition  $\{P_1, \dots, P_l\}$  of  $\mathcal{P}$ :

1. **Row by row:** set  $i = 0$ ,  $(a_0, b_0) := (0, 0)$  and  $P_1 := (a_0, b_0)$ . While  $|\mathcal{I}_{f, P_1, L}| \leq M$ , set

$$(a_{i+1}, b_{i+1}) := \begin{cases} (a_i + 1, b_i), & \text{if } a_i < P_x - 1, \\ (0, b_i + 1), & \text{otherwise} \end{cases}$$

and  $P_1 := P_1 \cup (a_{i+1}, b_{i+1})$ . Continue with  $P_2, \dots, P_l$  in the same fashion.

2. **Rectangles:** partition the set  $\mathcal{P}$  into rectangular sets  $P_1, \dots, P_l$  of the same size that are as large as possible while satisfying the condition  $|\mathcal{I}_{f, P_j, L}| \leq M$  at the same time; fill any remaining space with smaller rectangles. The order of the rectangles in the partition can be row-major or column-major.
3. **Greedy algorithm:** choose a random starting point  $(a_0, b_0)$  and set  $P_0 = (a_0, b_0)$ . New pixels are added to  $P_0$  by choosing the neighboring pixel  $(a_{i+1}, b_{i+1})$  to the previously added pixel  $(a_i, b_i)$  with the lowest cost, i.e. such that

$$|\mathcal{I}_{f, P_0, L} \cup \mathcal{I}_{f, (a_{i+1}, b_{i+1}), L}|$$

is minimal, where  $a_i - 1 \leq a_{i+1} \leq a_i + 1$  and  $b_i - 1 \leq b_{i+1} \leq b_i + 1$ . Continue for as long as possible while  $|\mathcal{I}_{f, P_0, L}| \leq M$  and then continue with  $P_1, P_2, \dots, P_l$  in the same way, starting with the last pixel that could not be added anymore to the previous set.

Figure 12 shows two examples for partitions computed with each of these three strategies. It is interesting to note that this approach doesn't necessarily increase the computation time: the partitions computed with the row by row and rectangle strategies in the second row of Figure 12 result in exactly the same number of Multislice calls as the trivial strategy  $P_1 = \mathcal{P}$ , but require significantly less computer memory. The partition computed with the rectangle strategy only requires storing about 1/4th of the Multislice results at any time as compared to the trivial strategy, reducing the required computer memory by 75% without increasing the computation time.

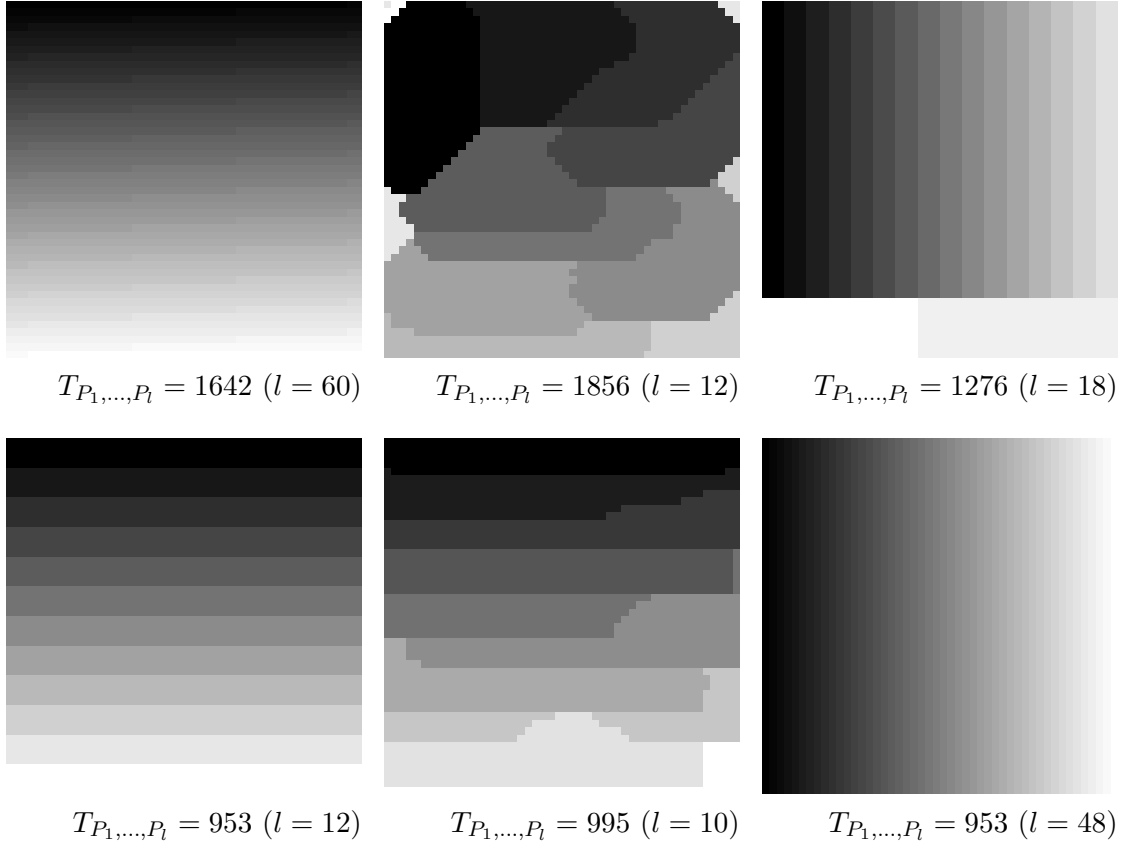


Figure 12: Two examples for partitions computed with the strategies row by row (left column), greedy (center column) and rectangle (right column). Different gray values correspond to different sets of the partition, where  $P_1$  consists of all black pixels and  $P_l$  of all white pixels. The minimum number of Multislice calls that can be achieved,  $T_{\mathcal{P}} = |\mathcal{I}_{f, \mathcal{P}, L}|$ , is 1077 (top row) respectively 953 (bottom row). Both experiments only differ in the target approximation error of the STEM probe, which is 0.01 for the experiment shown in the top row and 0.03 for the experiment in the bottom row, resulting in  $L = 75$  (approximation error 0.01) and  $L = 51$  (approximation error 0.03). The other parameters are  $u = \hat{\psi}_0^{\text{init}}$  and  $\mathcal{I} = \mathcal{P} + \frac{1}{2}(p_x, p_y)$  with  $f = 2$  and  $X = Y = 512$  as well as  $P_x = P_y = 158$ , where only a subsection of the STEM image of size  $48 \times 48$  was to be computed. The simulation window size is  $l_x = l_y = 31.208$  (in Angstrom) and the microscope settings are  $\lambda = 0.0250793$  (corresponding to an accelerating voltage of  $U = 200000$  Volt),  $Z = 100$ ,  $C_s = -2000$  and  $\alpha_{\text{max}} = 0.026$ .

### 4.2.5 Comparison of different input wave types

Figure 13 shows the simulation results for the M1 specimen [4, 1] with four different configurations of LMA. As expected from the results in Figure 11, the results look almost identical to the reference images in the top row, even though an relative approximation error of about 10% in the supremum norm was used in the simulation to keep  $L$  small and the simulation fast. The simulation of the images in the top row took about 24 hours, whereas the second row took 8 hours, the third row 12 hours and the fourth row 13 hours.

It is interesting to see the very different probe approximations that were used in these simulations as shown in Figure 14. In particular, well localized functions such as Gaussians or trigonometric polynomials only approximate the probes near their center. This will not yield a significant error in the output image as was already established by PRISM, where the results from the Multislice computations are cropped by a factor of  $f^2$  around the probe, which has a similar effect.

### 4.2.6 Recomputing local changes

One of the strong suits of the approach presented here is that the small support of the input waves in real space allows for a fast recomputation if local changes are made to the specimen such as changing a single atomic column. The reason for this is that we only need to redo those Multislice computations that are needed for the approximation of the probe positions close to the location of the local changes. If  $\mathcal{P}' \subseteq \mathcal{P}$  is the set of pixels of the STEM image that need to be recomputed, then the Multislice algorithm needs to be performed again only for those input wave positions in  $\mathcal{I}_{f,\mathcal{P}',L}$  that are close enough to the changes in the specimen to have the result of the Multislice computation changed.

In practice, this reduces the computation time twice: first, because we only need to recompute pixels within a small area around the changes; second, because we similarly only need to redo Multislice computations for input wave positions within a small area around the changes. While it is possible to compute individual pixels of the output image with PRISM, this always requires performing the Multislice algorithm for all input waves on the entire simulation window. MULTEM on the other hand requires performing the Multislice algorithm once for every probe position, providing no additional speedup.

Figure 15 shows an example where two configurations of the M1 specimen [4, 1] are simulated that differ only in one atomic column. In this example, the simulation window size is  $1024 \times 1024$  pixels with a physical size of  $84.536 \times 79.941$  Angstrom. The size of the probe lattice is  $(P_x, P_y) = (424, 400)$  and  $\mathcal{I} = \mathcal{P} + \frac{1}{2}(p_x, p_y)$  with  $f = 2$ . The maximum relative approximation error in the supremum norm in this example is set to 2%, which results in  $L = 59$  when computing the approximation coefficients with linear least squares.

For the images shown in the left column of Figure 15, this results in  $P_x P_y = 169600$  probe positions and an overall number of  $|\mathcal{I}_f| = 212 \cdot 200 = 42400$  times that the Multislice algorithm needs to be performed. If one was then interested in changes in

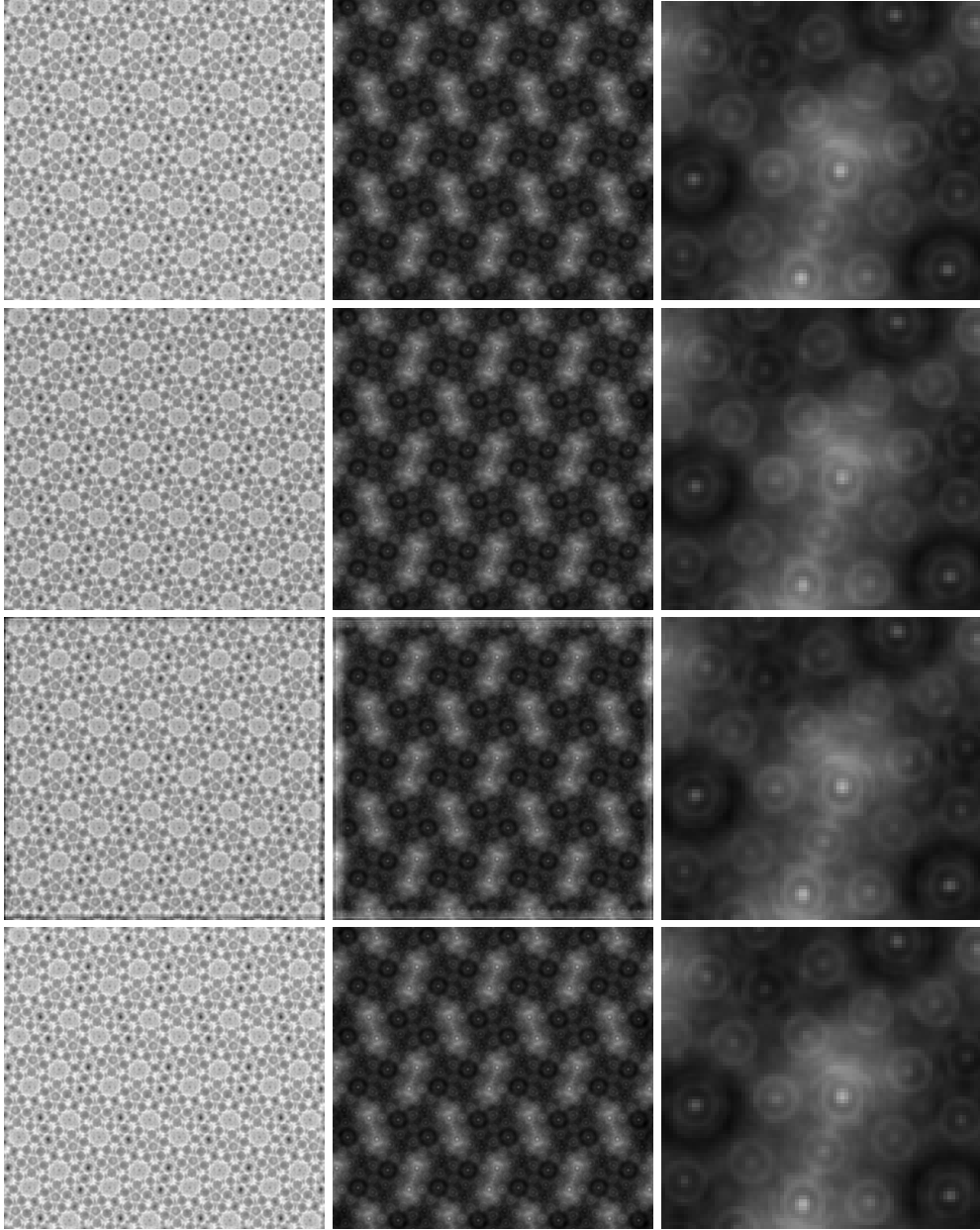


Figure 13: Simulated images of the M1 specimen with the LMA algorithm and four different configurations. Top row:  $u = \hat{\psi}_0^{\text{init}}$  with  $\mathcal{I} = \mathcal{P}$ ,  $f = 1$  and  $L = 1$ . Second row:  $u = \hat{\psi}_0^{\text{init}}$  with  $\mathcal{I} = \mathcal{P} + \frac{1}{2}(p_x, p_y)$ ,  $f = 2$  and  $L = 27$ . Third row:  $u(x, y) = \varphi_n(x)\varphi_n(y)$  with  $\mathcal{I} = \mathcal{P} + \frac{1}{2}(p_x, p_y)$ ,  $f = 2$  and  $L = 283$ . Bottom row:  $u = g_\sigma$  with  $\sigma = 0.482$  Angstrom,  $\mathcal{I} = \mathcal{P} + \frac{1}{2}(p_x, p_y)$ ,  $f = 2$  and  $L = 379$ . Left column: BF images ( $[r_1, r_2] = [0, 15]$ ). Middle column: HAADF images ( $[r_1, r_2] = [41, 200]$ ). Right column: subsection of the HAADF images. The relative probe approximation errors in the supremum norm are 0% for the top row and about 10% for the other rows.

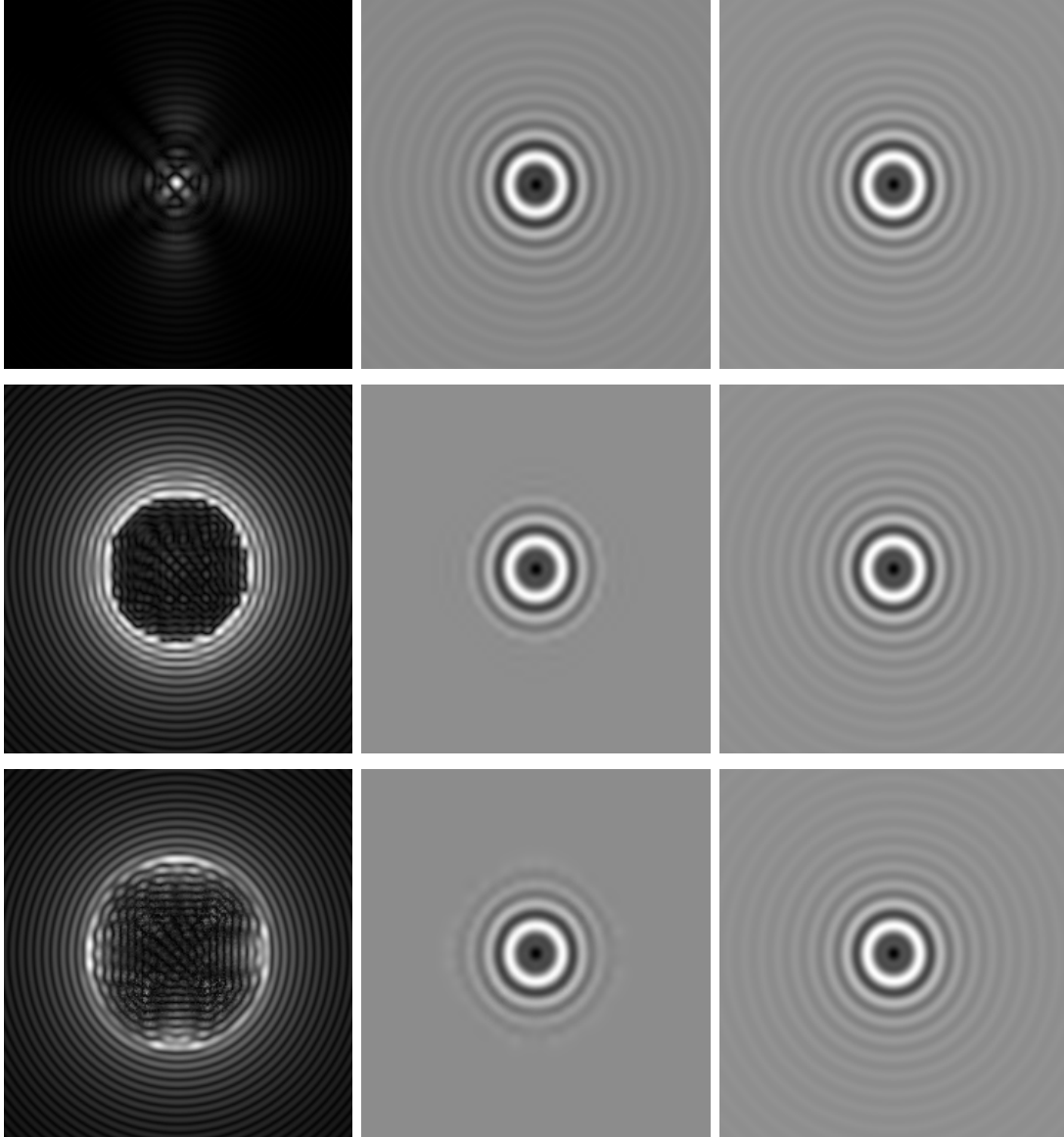


Figure 14: Approximations of the STEM probes corresponding to the second, third and fourth row of Figure 13. Top row:  $u = \hat{\psi}_0^{\text{init}}$ . Middle row:  $u(x, y) = \varphi_n(x)\varphi_n(y)$ . Bottom row:  $u = g_\sigma$  with  $\sigma = 0.482$  Angstrom. Left column: relative errors in the supremum norm, where white equals 10% and black equals 0%. Middle column: Imaginary part of the resulting approximation of the STEM probe. Right column: imaginary part of the STEM probe.

the intensity if only the atomic column depicted by the red arrow in Figure 15 was changed, it would be a waste to repeat the entire computation. Instead, using the approach outlined above, only 11554 probe positions need to be recomputed, which requires the recomputation of 3825 Multislice solutions. In our experiment, this reduced the computation time from 150 minutes to 14 minutes for every image after the initial one.

**Source code:** the source code that implements LMA and has been used for all experiments in this paper is made freely available at <https://github.com/CDoberstein/LMA>.

**Acknowledgments:** The authors thank Thomas Vogt, Douglas Blom and Michael Matthews for helpful discussions on the research in this paper.

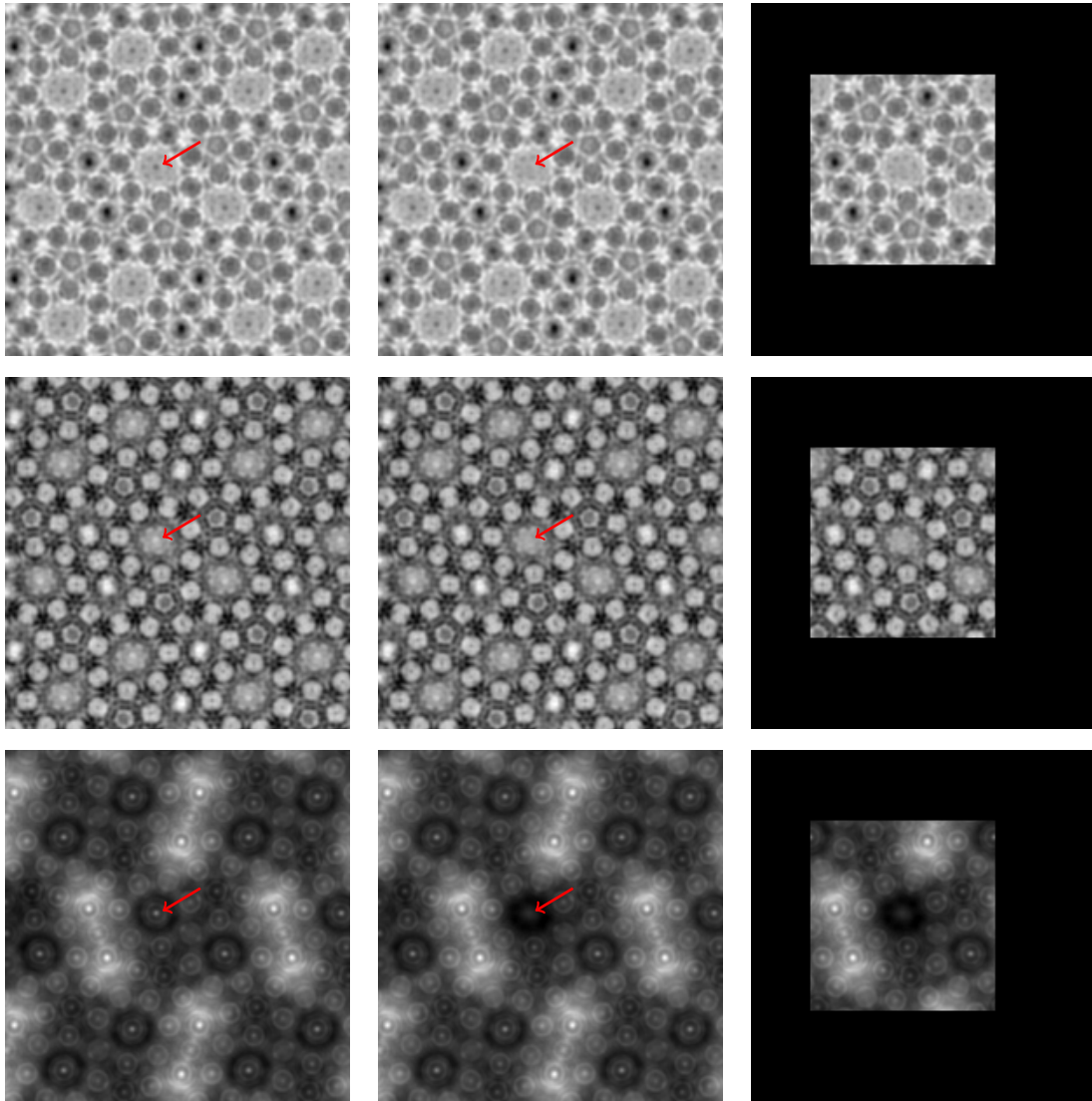


Figure 15: STEM images of the M1 specimen simulated with LMA. Top row: bright field ( $[r_1, r_2] = [0, 15]$ ); middle row: annular dark field ( $[r_1, r_2] = [16, 40]$ ); bottom row: high angle annular dark field ( $[r_1, r_2] = [41, 200]$ ). The images in the left and middle column only differ by changes to the atomic column indicated by the red arrow. For the images in the left column, the atomic column consists of alternating Te and O atoms, whereas all Te atoms have been replaced by O atoms for the image in the middle column. The images in the right column show those pixels that had to be recomputed, i.e. the images in the middle column are a combination of the images in the left and right column. Shown here are cropped subsections of the specimen for a better visibility of the differences between the images.

## References

- [1] D. A. Blom and T. Vogt. Multi-slice frozen phonon simulations of high-angle annular dark field scanning transmission electron microscopy images of the structurally and compositionally complex Mo–V–Nb–Te oxide catalyst. *Adv Struct Chem Imag*, 4(9), 2018. <https://doi.org/10.1186/s40679-018-0058-5>.
- [2] J. M. Cowley and A. F. Moodie. The Scattering of Electrons by Atoms and Crystals. I. A New Theoretical Approach. *Acta Cryst.*, 10:609 – 619, 1957. <https://doi.org/10.1107/S0365110X57002194>.
- [3] L. R. DaCosta, H. G. Brown, P. M. Pelz, A. Rakowski, N. Barber, P. O’Donovan, P. McBean, L. Jones, J. Ciston, M. C. Scott, and C. Ophus. Prismatic 2.0 – Simulation software for scanning and high resolution transmission electron microscopy (STEM and HRTEM). *Micron*, 151:103141, 2021. <https://doi.org/10.1016/j.micron.2021.103141>.
- [4] P. DeSanto, D. J. Buttrey, R. K. Grasselli, C. G. Lugmair, A. F. Volpe, B. H. Toby, and T. Vogt. Structural aspects of the M1 and M2 phases in MoVNbTeO propane ammoxidation catalysts. *Z. Kristallogr*, 219:152 – 165, 2004. <https://doi.org/10.1524/zkri.219.3.152.29091>.
- [5] A. Pryor Jr., C. Ophus, and J. Miao. A streaming multi-GPU implementation of image simulation algorithms for scanning transmission electron microscopy. *Adv Struct Chem Imag*, 3(15), 2017. <https://doi.org/10.1186/s40679-017-0048-z>.
- [6] E. J. Kirkland. *Advanced Computing in Electron Microscopy*. Springer, 2nd edition, 2010. <https://doi.org/10.1007/978-1-4419-6533-2>.
- [7] E. J. Kirkland. Computation in electron microscopy. *Acta Cryst.*, A72:1 – 27, 2016. <https://doi.org/10.1107/S205327331501757X>.
- [8] I. Lobato, S. Van Aert, and J. Verbeeck. Progress and new advances in simulating electron microscopy datasets using MULTEM. *Ultramicroscopy*, 168:17 – 27, 2016. <https://doi.org/10.1016/j.ultramic.2016.06.003>.
- [9] I. Lobato and D. Van Dyck. MULTEM: A new multislice program to perform accurate and fast electron diffraction and imaging simulations using Graphics Processing Units with CUDA. *Ultramicroscopy*, 156:9 – 17, 2015. <https://doi.org/10.1016/j.ultramic.2015.04.016>.
- [10] J. O. Oelerich, L. Duschek, J. Belz, A. Beyer, S. D. Baranovskii, and K. Volz. STEM-salabim: A high-performance computing cluster friendly code for scanning transmission electron microscopy image simulations of thin specimens. *Ultramicroscopy*, 177:91 – 96, 2017. <https://doi.org/10.1016/j.ultramic.2017.03.010>.

- [11] C. Ophus. A fast image simulation algorithm for scanning transmission electron microscopy. *Adv Struct Chem Imag*, 3(13), 2017. <https://doi.org/10.1186/s40679-017-0046-1>.
- [12] H. Rauhut. Best time localized trigonometric polynomials and wavelets. *Advances in Computational Mathematics*, 22:1 – 20, 2005. <https://doi.org/10.1007/s10444-005-7411-7>.